

A statistically stationary minimal flow unit for self-similar Rayleigh–Taylor turbulence in the mode-coupling limit

Chian Yeh Goh¹† and Guillaume Blanquart¹

¹California Institute of Technology, Pasadena, CA 91125, USA

(Received 5 June 2024; revised 12 November 2024; accepted 15 November 2024)

We propose a computational framework for simulating the self-similar regime of turbulent Rayleigh–Taylor (RT) mixing layers in a statistically stationary manner. By leveraging the anticipated self-similar behaviour of RT mixing layers, a transformation of the vertical coordinate and velocities is applied to the Navier–Stokes equations (NSE), yielding modified equations that resemble the original NSE but include two sets of additional terms. Solving these equations, a statistically stationary RT (SRT) flow is achieved. Unlike temporally growing Rayleigh–Taylor (TRT) flow, SRT flow is independent of initial conditions and can be simulated over infinite simulation time without escalating resolution requirements, hence guaranteeing statistical convergence. Direct numerical simulations (DNS) are performed at an Atwood number of 0.5 and unity Schmidt number. By varying the ratio of the mixing layer height to the domain width, a minimal flow unit of aspect ratio 1.5 is found to approximate TRT turbulence in the self-similar mode-coupling regime. The SRT minimal flow unit has one-sixteenth the number of grid points required by the equivalent TRT simulation of the same Reynolds number and grid resolution. The resultant flow corresponds to a theoretical limit where self-similarity is observed in all fields and across the entire spatial domain – a late-time state that existing experiments and DNS of TRT flow have difficulties attaining. Simulations of the SRT minimal flow unit span TRT-equivalent Reynolds numbers (based on mixing layer height) ranging from 500 to 10 800. The SRT results are validated against TRT data from this study as well as from Cabot & Cook (*Nat. Phys.*, vol. 2, 2006, pp. 562–568).

Key words: buoyancy-driven instability, turbulence simulation, turbulent mixing

† Email address for correspondence: cgoh@caltech.edu

1. Introduction

Buoyancy-driven turbulent flows occur in many natural phenomena and engineering applications, including astrophysics, earth sciences, inertial confinement fusion and combustion systems. An extensive list of many such examples can be found in the review article by Zhou (2017a). Often, these flows involve the complex coupling of many physical phenomena such as buoyancy, combustion, multiphase interactions and shocks. Direct numerical simulation (DNS) of turbulent flows is prohibitively expensive and practically impossible for most applications, and flow modelling is necessary to account for the unresolved parts of the flow. To aid the development of such models, various flow physics can be isolated using canonical problems. Such problems afford scientists deeper physical understanding of the flow physics and also function as computationally tractable validation test beds for model development.

The Rayleigh–Taylor instability (Rayleigh 1882; Taylor 1950) occurs between fluids of different densities, when the light fluid is accelerated into the heavy by an external pressure gradient. A canonical flow configuration used extensively to study such instabilities is the planar Rayleigh–Taylor (RT) flow configuration. Two fluids of different densities are initially separated by a planar interface in an unstable configuration and accelerated by a constant gravitational force normal to the interface. The RT configuration has been studied extensively, and many of the key contributions are summarized in several review articles. Zhou (2017a,b) contains a comprehensive overview of RT-related research, while more focused reviews on theoretical modelling (Abarzhi 2010), RT turbulence in the Boussinesq limit (Boffetta & Mazzino 2017) and experiments (Andrews & Dalziel 2010; Banerjee 2020) also exist. Finally, Schilling (2020) summarizes efforts and potential opportunities for integrating simulation, modelling and experiments.

1.1. Rayleigh–Taylor instability

In the canonical RT configuration, a heavy fluid sits atop a light fluid in the presence of a constant acceleration field, such as gravity. The flow is initially stationary, and pure reservoirs of heavy and light miscible fluid are separated by an infinitely thin and flat interface situated at $x_2 = \delta_I$. These initial conditions are

$$\rho(t = 0, \mathbf{x}) = \begin{cases} \rho_L, & x_2 < \delta_I, \\ \rho_H, & x_2 > \delta_I, \end{cases} \quad (1.1)$$

$$\mathbf{u}(t = 0, \mathbf{x}) = 0, \quad (1.2)$$

where ρ is the density and \mathbf{u} the velocity. The subscripts H and L indicate the properties of the heavy and light fluids, respectively. Gravity acts vertically downwards, i.e. $g_i = -g\delta_{2i}$.

In the presence of small perturbations at the interface, RT instabilities develop. Linear stability analysis predicts exponential growth at all wavelengths in the inviscid limit (Rayleigh 1882; Taylor 1950), while viscosity (Chandrasekhar 1955) and diffusivity (Duff, Harlow & Hirt 1962) have been found to inhibit small-scale growth. As perturbations grow, nonlinearities become important and the flow undergoes a transition to turbulence.

1.2. Self-similarity in turbulent Rayleigh–Taylor flows

As the flow transitions to turbulence, it is widely believed that an asymptotic self-similar regime exists. In this regime, Youngs (1984) observed a quadratic growth of the mixing

Quantity	Definition
Mixing height	$h_m = \frac{4}{\rho_0} \int \langle \rho Y(1 - Y) \rangle dx_2$
Product height	$h_p = 2 \int \min(\langle X \rangle, \langle 1 - X \rangle) dx_2$
Bubble height	$H_b = x_2(\langle X \rangle = 0.99) - \delta_I$
Spike height	$H_s = \delta_I - x_2(\langle X \rangle = 0.01)$
Threshold height	$H = H_b + H_s$
Entrainment height	$h_1 = 4 \int \langle X \rangle (1 - \langle X \rangle) dx_2$

Table 1. Different definitions of the mixing layer height. Here, X and Y are the mole and mass fractions of the heavy fluid; $\rho_0 = 2\rho_H\rho_L/(\rho_H + \rho_L)$ is a normalization density; δ_I is the initial interface location. All integrals in x_2 are taken from $x_2 = -\infty$ to $x_2 = +\infty$.

layer height, $h \approx \alpha A g t^2$. By applying similarity assumptions to the governing equations, Ristorcelli & Clark (2004) derived an equivalent result

$$\dot{h}^2 = 4\alpha A g h, \quad (1.3)$$

where $h(t)$ is a mixing layer height, $\dot{h} = dh/dt$, $A = (\rho_H - \rho_L)/(\rho_H + \rho_L)$ is the Atwood number and α is a dimensionless growth parameter. Although the relationship $\dot{h}^2 \propto h$ is valid for any height definition, the specific value of α depends on the choice of height definition. All height definitions used in this paper are listed in table 1.

Self-similarity in RT flows is typically demonstrated by stationarity in normalized statistics. For example, the growth parameter α is commonly used as evidence of self-similarity, as are various measures of mixedness (Zhou, Cabot & Thornber 2016). For planar-averaged quantities that vary along the vertical direction, data from different simulation times should collapse onto each other when normalized suitably. Typically, the vertical coordinate is normalized by the height of the mixing layer h , and self-similarity has been demonstrated with various height definitions. Velocities can be scaled with h (e.g. Zhou & Cabot 2019) or $(gh)^{1/2}$ (e.g. Vladimirova & Chertkov 2009). Equivalently, the total kinetic energy of the flow can be scaled by the potential energy loss of the flow (e.g. Cabot & Cook 2006). These velocity scalings are all consistent, by virtue of (1.3).

This self-similar growth is commonly associated with three conditions that are satisfied by late-time RT flow (Youngs 1984; Cook, Cabot & Miller 2004).

- In an infinitely large domain, the mixing layer height $h(t)$ eventually becomes much larger than any characteristic length scale of the initial interface perturbations ℓ_I . When $h(t) \gg \ell_I$, the flow loses memory of its initial conditions, and flow structures grow in size solely through the merger of smaller structures (or mode-coupling processes).
- The flow transitions to turbulence, and widening scale separation between the buoyancy-driven large scales and the viscous/diffusive small scales leads to $h(t) \gg \eta$, where η is the Kolmogorov length scale commonly used to characterize the small turbulence scales. An equivalent condition can be stated in terms of the Reynolds number. For RT flow, the mixing layer Reynolds number can be defined as

$$Re = \frac{H\dot{H}}{\nu}, \quad (1.4)$$

where $H(t)$ is defined in table 1, $\dot{H} = dH/dt$ and ν is the kinematic viscosity. This definition was chosen to be consistent with Cabot & Cook (2006), which will be used

as a recurring reference for comparison in this paper. For the flow to be turbulent, $Re(t) \gg 1$.

(iii) In an infinite three-dimensional domain, when $h(t) \gg \ell_I, \eta$, the mixing layer evolution is fully characterized by its height and the flow is self-similar. However, in practice, any experiment or simulation must be performed on a domain of a finite size \mathcal{L} . Obviously, vertical boundaries should be much larger than $h(t)$. Additionally, confinement effects from the lateral domain boundaries also modify the qualitative nature of RT turbulence (Dalziel *et al.* 2008; Boffetta, De Lillo & Musacchio 2012a; Boffetta *et al.* 2012b). Hence, to approximate RT mixing layer growth in an infinite domain, the third condition for finite-domain RT flows is $h(t) \ll \mathcal{L}$.

Summarily, these three conditions can be stated as

$$\ell_I, \eta \ll h(t) \ll \mathcal{L}. \quad (1.5)$$

The difficulty in satisfying the contradicting requirements of (i) and (iii) is well illustrated by the discrepancies in observed α values between experiments and simulations (Dimonte *et al.* 2004; Boffetta & Mazzino 2017). Using a bubble height definition, experiments consistently yield α values in the range of 0.05–0.08, while simulations produce smaller values of 0.02–0.03. This has been attributed to differences in wavelength content of the initial perturbations. Specifically, Ramaprabhu & Andrews (2004b) and Mueschke & Schilling (2009a,b) simulated RT growth using experimentally measured initial conditions and successfully reproduced larger α values comparable to those from experiments. Other numerical studies (Ramaprabhu, Dimonte & Andrews 2005; Banerjee & Andrews 2009; Youngs 2013) have also confirmed that smaller (respectively larger) α values are observed when initial perturbations are applied only at the smallest scales (respectively over a wide range of scales). This paper focuses solely on the late-time, infinite-domain limit described by (1.5), also known as the mode-coupling (Ramaprabhu *et al.* 2005; Youngs 2013) or ‘ideal’ (Zhou 2017a) case. Any subsequent mention of self-similar RT growth in this paper refers specifically to this case.

It is worth clarifying that the typical interpretation of self-similarity in turbulent RT flows does not imply that all quantities are statistically stationary when normalized with a single set of normalization scales. At the large scales, viscosity and diffusivity have no effect, and all large-scale quantities can be normalized by A , g and h . The specific interpretation of self-similarity used in this paper is: (a) all quantities demonstrate statistical stationarity when normalized appropriately; (b) specifically, the large-scale dynamics is buoyancy driven, and the appropriate normalization of the large scales involves length scale h , and time scale $(h/Ag)^{1/2}$.

The relative importance of conditions (i) and (ii) is also an open question. As an RT flow evolves in time, its memory of the initial conditions fades and its Reynolds number increases. Both conditions are consistent with the observation that self-similarity is approached at late times. However, both conditions are intrinsically linked in temporally evolving RT flows and cannot be studied independently. In particular, no minimum threshold Reynolds number has been established for the existence of self-similar RT behaviour, nor is there a framework for assessing how long a given initial condition would take to be sufficiently forgotten.

From a modelling perspective, self-similarity is an assumption utilized by many Reynolds-averaged Navier–Stokes models to reduce the complexity of the RT governing equations (Dimonte & Tipton 2006; Banerjee, Gore & Andrews 2010a; Morgan & Wickett 2015; Schilling 2021). To derive analytical forms of the self-similar fields and calibrate model coefficients, accurate data of high Re self-similar RT turbulence are required.

The challenges associated with such efforts are discussed in Schilling (2021). Direct numerical simulation has been used to provide modelling insights (Livescu *et al.* 2009; Schilling & Mueschke 2010, 2017), but sources of high Re self-similar RT data are rare, and it remains questionable if any have reached full self-similarity.

1.3. Rayleigh–Taylor and other related configurations

Due to challenges in imposing suitable initial perturbations, experiments have had limited success in producing self-similar mode-coupling RT turbulence. Direct numerical simulation is a viable, but costly, alternative. Compromising some accuracy for tractability, large eddy simulation (LES) is commonly used in RT studies. Most LES studies use implicit LES (Dimonte *et al.* 2004 and references therein) or artificial fluid models (Cook *et al.* 2004); only a few employ explicit subgrid-scale models (Mellado, Sarkar & Zhou 2005; Burton 2011; Yilmaz 2020; Luo *et al.* 2023). Further, with the exception of Cook *et al.* (2004) and Luo *et al.* (2023), there seems to be limited effort in LES validation with DNS results, perhaps due to the difficulty in obtaining DNS results in the first place. In summary, DNS studies remain critical for the physical understanding of RT turbulence. There have been several DNS of non-Boussinesq RT flows (Cabot & Cook 2006; Livescu, Wei & Petersen 2011; Cabot & Zhou 2013) covering Atwood numbers up to 0.9, but these are costly to repeat for comprehensive parametric studies.

There are multiple reasons for the large computational cost associated with DNS of RT flows. First, the desired high Reynolds number and self-similar flow conditions are often only met near the end of the simulation. Practically, this final state dictates the domain size and grid requirements. Yet, a large fraction of the computational time is spent in the early stages that are significantly less turbulent. Second, it is not possible to obtain multiple data snapshots at a single flow condition due to the time-dependent nature of RT turbulence. While one could choose to obtain temporal statistics over a finite range of Reynolds numbers (e.g. by collecting statistics on similarity variables), this approach would require simulations to be performed to a final Reynolds number larger than the target value. Lastly, although the late-time RT behaviour of interest is independent of initial conditions, the nature and extent of the preceding transition is highly dependent on initial conditions, making it a challenge to plan for an efficient use of computational resources *a priori*. Much of the cost associated with RT simulations is unavoidable in practice but scientifically redundant.

A temporally growing RT layer, as described in § 1.1, is non-stationary and homogeneous in two directions. A statistically stationary variant that is found in gas tunnel/water channel experiments (Ramaprabhu & Andrews 2004a; Banerjee & Andrews 2006; Mueschke, Andrews & Schilling 2006; Mueschke *et al.* 2009; Banerjee, Kraft & Andrews 2010b; Mikhaeil *et al.* 2021) and related simulations (Mueschke & Schilling 2009a) involves the convection of a mixing layer downstream by a uniform flow. While statistical stationarity can enhance the quality of ensemble statistics by providing more flow realizations, the development time of the mixing layer remains constrained by domain size. The two main issues of domain size constraints and sensitivity to initial conditions remain unresolved.

To circumvent these challenges, simplified configurations of varying flavours have been proposed to represent the core of the RT mixing layer (Livescu & Ristorcelli 2007; Chung & Pullin 2010; Carroll & Blanquart 2015), but these studies generate density fluctuations through non-physical source terms or arbitrary initial conditions. The actual source of mean density gradients in RT flow, the two pure fluid reservoirs, is not physically present in any of these configurations – an issue that the present work seeks to rectify. A summary of the differences between these configurations and the current work is presented in table 2.

Study/Configuration	#HD	Stationarity	Source of density variance
Temporally growing RT (Cabot & Cook 2006)	2	No	Pure fluid reservoirs
Spatially growing RT (Mueschke & Schilling 2009a)	1	Yes	Pure fluid reservoirs
Livescu & Ristorcelli (2007)	3	No	Initial conditions
Chung & Pullin (2010)	2	Yes	Source terms in fringe region
Carroll & Blanquart (2015)	3	Yes	Linear scalar forcing
Stationary RT (current work)	2	Yes	Pure fluid reservoirs

Table 2. Rayleigh–Taylor-related configurations and representative studies (#HD: number of homogeneous directions).

1.4. Objectives

This paper proposes a statistically stationary RT configuration, where the mixing layer height is approximately constant, and the boundary conditions are consistent with the temporally growing RT configuration. To achieve statistical stationarity, we solve the RT governing equations in terms of similarity variables, extending an approach by Ruan & Blanquart (2021) that transforms spatially developing boundary layers into streamwise homogeneous ones. In this case, we transform a temporally evolving flow into a statistically stationary one. We refer to these flow configurations as TRT (for ‘temporally growing RT’) and SRT (for ‘statistically stationary RT’). We expect SRT flow to be representative of self-similar TRT flow, independent of initial conditions, and stationary at all scales. By eliminating the effect of initial conditions, the sensitivity of RT self-similarity to Reynolds number can be studied independently, addressing an open question raised in § 1.2. Additionally, flow stationarity should help bypass many of the computational challenges associated with DNS of TRT flows, as discussed in § 1.3.

This paper is organized as follows. Section 2 details the derivation of the governing equations, and § 3 explains the choice of inputs to these equations. Section 4 addresses numerical implementation and documents the full list of simulation cases performed. The results are divided into two sections. Section 5 demonstrates characteristics of the SRT framework, and § 6 reports insights into RT flow physics that are gathered from SRT simulations. Section 7 compares SRT and TRT configurations from several broad perspectives. Lastly, some concluding remarks are made in § 8.

2. Governing equations

In § 2.1, the governing equations and boundary conditions for a TRT flow are presented. Several integral flow quantities of interest are introduced. Then, the governing equations are transformed through a coordinate rescaling and simplified to the SRT governing equations in § 2.2. Finally, § 2.3 examines the stationary solution of the SRT configuration.

2.1. Temporally growing Rayleigh–Taylor mixing layer

2.1.1. Low-Mach-number Navier–Stokes equations

The low-Mach-number Navier–Stokes equations (NSE) govern the evolution of RT flows. The equations for continuity, momentum and scalar transport are

$$\frac{\partial \rho}{\partial t} + \frac{\partial \rho u_j}{\partial x_j} = 0, \quad (2.1)$$

$$\frac{\partial \rho u_i}{\partial t} + \frac{\partial \rho u_i u_j}{\partial x_j} = -\frac{\partial p}{\partial x_i} + \frac{\partial \tau_{ij}}{\partial x_j} - \rho g \delta_{2i}, \quad (2.2)$$

$$\frac{\partial \rho Y}{\partial t} + \frac{\partial \rho Y u_j}{\partial x_j} = \frac{\partial}{\partial x_j} \left(\rho D \frac{\partial Y}{\partial x_j} \right), \quad (2.3)$$

where p is the hydrodynamic pressure, τ_{ij} the shear stress tensor, Y the mass fraction of the heavy fluid and D the kinematic diffusivity. The shear stress tensor is defined as

$$\tau_{ij} = \rho \nu \left(\frac{\partial u_i}{\partial x_j} + \frac{\partial u_j}{\partial x_i} - \frac{2}{3} \frac{\partial u_k}{\partial x_k} \delta_{ij} \right), \quad (2.4)$$

where ν is the kinematic viscosity and δ_{ij} the Kronecker delta.

In the low-Mach-number formulation, the ideal gas equation of state is

$$\rho = \frac{P_0 W}{R T}, \quad (2.5)$$

where P_0 is a constant background pressure, W the molecular weight of the mixture, R the universal gas constant and T the mixture temperature. Density differences may arise from the mixing of two fluids of different molecular weights, $1/W = Y/W_H + (1 - Y)/W_L$, or different temperatures, $T = Y T_H + (1 - Y) T_L$. Substituting either relation into (2.5) leads to the same result: the mixture density is uniquely determined by the mass fraction, i.e.

$$\rho(Y) = \frac{\rho_H \rho_L}{\rho_H - (\rho_H - \rho_L)Y} \quad \text{or} \quad Y(\rho) = \frac{\rho_H(\rho - \rho_L)}{\rho(\rho_H - \rho_L)}. \quad (2.6a,b)$$

2.1.2. Boundary conditions

The flow is statistically homogeneous in the x_1 and x_3 directions, which can be stated as

$$\frac{\partial \langle \cdot \rangle}{\partial x_1} = \frac{\partial \langle \cdot \rangle}{\partial x_3} = 0, \quad (2.7)$$

where $\langle \cdot \rangle$ denotes any ensemble-averaged quantity of the flow. Computationally, (2.7) is implemented as periodic boundary conditions in x_1 and x_3 . The boundary conditions representing the two infinite fluid reservoirs are

$$\mathbf{u}(x_2 \rightarrow \pm\infty) = 0, \quad (2.8)$$

$$\rho(x_2 \rightarrow -\infty) = \rho_L, \quad \rho(x_2 \rightarrow +\infty) = \rho_H, \quad (2.9a,b)$$

$$Y(x_2 \rightarrow -\infty) = 0, \quad Y(x_2 \rightarrow +\infty) = 1. \quad (2.10a,b)$$

Additionally, the derivatives of \mathbf{u} , ρ and Y are zero as $x_2 \rightarrow \pm\infty$. Evaluating (2.2) in the limit of $x_2 \rightarrow \pm\infty$, the boundary conditions for pressure are

$$\frac{\partial p}{\partial x_2}(x_2 \rightarrow -\infty) = -\rho_L g, \quad \frac{\partial p}{\partial x_2}(x_2 \rightarrow +\infty) = -\rho_H g. \quad (2.11a,b)$$

2.1.3. Integral flow quantities

To track RT layer growth, several integral flow quantities are defined, and their time evolution is derived. First, the change in total mass of the system is considered using

$$\delta_I(t) = \frac{1}{\rho_H - \rho_L} \left(\int_0^{+\infty} (\rho_H - \langle \rho \rangle) dx_2 + \int_{-\infty}^0 (\rho_L - \langle \rho \rangle) dx_2 \right). \quad (2.12)$$

If the total mass of the system is hypothetically rearranged into two pure fluid reservoirs of ρ_H and ρ_L that are separated by an infinitely thin interface, then δ_I is the vertical location of this interface. Analogous to the displacement thickness in boundary layers, δ_I is a displacement length that measures how much the mass of the system is displaced from one with an initial interface at $x_2 = 0$. A positive (upward) shift of δ_I represents mass loss, while a negative shift indicates mass gain.

The time evolution of δ_I can be derived from the ensemble-averaged continuity equation, which is written as

$$\frac{\partial \langle \rho \rangle}{\partial t} + \frac{\partial \langle \rho u_2 \rangle}{\partial x_2} = 0, \quad (2.13)$$

where statistical homogeneity in x_1 and x_3 has been applied. Taking the time derivative of (2.12), substituting (2.13) and applying the velocity boundary conditions (2.8) results in

$$\frac{d\delta_I}{dt} = 0. \quad (2.14)$$

This implies that mass is globally conserved in a TRT flow.

Next, we consider the mixing height

$$h_m(t) = \frac{4}{\rho_0} \int_{-\infty}^{+\infty} \langle \rho Y(1 - Y) \rangle dx_2, \quad (2.15)$$

where $\rho_0 = 2\rho_H\rho_L/(\rho_H + \rho_L)$ is a normalization density chosen to be the harmonic mean of the maximum and minimum densities (it is also the mixture density evaluated at $Y = 0.5$). Unlike other height definitions (e.g. h_p , H) that measure the extent of fluid entrainment, h_m measures the extent of fluid mixing; h_m can be related to entrainment heights using closure models for the turbulence fluctuations (Zhang *et al.* 2020), but this is not generally possible without some simplifications. For additional context, (2.15) is similar to the definition of the total mixed mass in Zhou *et al.* (2016), but with an additional density normalization.

By including density within the averaging operator of (2.15), a simple and physically intuitive expression is obtained for the growth of h_m . To derive this expression, the scalar transport equation, (2.3), is first multiplied by $2Y$ and simplified using continuity to get

$$\frac{\partial \rho Y^2}{\partial t} + \frac{\partial \rho Y^2 u_j}{\partial x_j} = \frac{\partial}{\partial x_j} \left(\rho D \frac{\partial Y^2}{\partial x_j} \right) + 2\rho D \left(\frac{\partial Y}{\partial x_j} \right)^2. \quad (2.16)$$

Then, a transport equation for the local mixed mass, $m = Y(1 - Y)$, is derived by subtracting (2.16) from (2.3). The resulting equation is ensemble averaged to yield

$$\frac{\partial \langle \rho m \rangle}{\partial t} = -\frac{\partial \langle \rho m u_2 \rangle}{\partial x_2} + \frac{\partial}{\partial x_2} \left\langle \rho D \frac{\partial m}{\partial x_2} \right\rangle + \langle \rho \chi \rangle, \quad (2.17)$$

where $\chi = 2D(\partial Y/\partial x_j)^2$ is the local scalar dissipation rate. Spatial derivatives in x_1 and x_3 are eliminated by homogeneity. Finally, integrating (2.17) over x_2 yields

$$\frac{dh_m}{dt} = \frac{4}{\rho_0} \underbrace{\int_{-\infty}^{+\infty} \langle \rho \chi \rangle dx_2}_{\Phi_\chi}. \quad (2.18)$$

In the derivation of (2.18), the convective and diffusive terms are eliminated because $m(x_2 \rightarrow \pm\infty) = 0$. The remaining term scales directly with the scalar dissipation integral Φ_χ and is strictly non-negative. Analytically, (2.18) shows that h_m increases monotonically with time as a result of diffusive processes, a result consistent with observations made by Zhou *et al.* (2016) on the total mixed mass.

Finally, the implications of flow self-similarity are considered. For a self-similar TRT flow, all integral flow dynamics can be fully parameterized by a single length scale. This can be any height definition (table 1). Self-similarity implies that these time-varying height definitions vary proportionally to each other. As a consequence,

$$\frac{1}{h_m} \frac{dh_m}{dt} = \frac{1}{h_i} \frac{dh_i}{dt}. \quad (2.19)$$

2.2. Statistically stationary Rayleigh–Taylor mixing layer

This section details the derivation of a modified set of equations that governs the SRT configuration. This includes a coordinate transformation of the NSE based on its large-scale similarity variables and additional simplifying assumptions.

2.2.1. Transformation of the low-Mach Navier–Stokes equations

We apply a coordinate transformation from x_i to ξ_i , which includes a shift by $\delta(t)$ followed by a scaling of the vertical spatial coordinate by $q(t)$. Velocity is scaled from u_i to u_i^* using the time derivative of q . This transformation is stated mathematically as

$$s = t, \quad \xi_1 = x_1, \quad \xi_2 = \frac{q_0}{q(t)}[x_2 - \delta(t)], \quad \xi_3 = x_3, \quad (2.20a-d)$$

$$u_i^* = u_i \frac{q'_0}{q'(t)}, \quad \frac{\partial p^*}{\partial \xi_i} = \frac{\partial p}{\partial x_i}, \quad Y^* = Y, \quad (2.21a-c)$$

where $q_0 = q(t_0)$ and $q'_0 = q'(t_0)$ are normalization constants yet to be determined. To simplify notation, primes denote time derivatives, e.g. $q' = dq/dt$. The partial derivative operators can be expressed in terms of the rescaled variables as

$$\frac{\partial}{\partial t} = \frac{\partial}{\partial s} - \left(\frac{q'(t)}{q(t)} \xi_2 + \frac{q_0}{q(t)} \delta'(t) \right) \frac{\partial}{\partial \xi_2}, \quad \frac{\partial}{\partial x_i} = \frac{\partial}{\partial \xi_i} - \delta_{2i} \left(1 - \frac{q_0}{q(t)} \right) \frac{\partial}{\partial \xi_2}. \quad (2.22a,b)$$

Substituting (2.20)–(2.22) into the low-Mach governing equations, we get

$$\frac{\partial \rho^*}{\partial s} + \frac{\partial \rho^* u_j^*}{\partial \xi_j} = \left(\frac{q'}{q} \xi_2 + \frac{q_0}{q} \delta' \right) \frac{\partial \rho^*}{\partial \xi_2} + H_{c,1}, \quad (2.23)$$

$$\begin{aligned} \frac{\partial \rho^* u_i^*}{\partial s} + \frac{\partial \rho^* u_i^* u_j^*}{\partial \xi_j} = & - \frac{\partial p^*}{\partial \xi_i} + \frac{\partial \tau_{ij}^*}{\partial \xi_j} - \rho^* g \delta_{2i} + \left(\frac{q'}{q} \xi_2 + \frac{q_0}{q} \delta' \right) \frac{\partial \rho^* u_i^*}{\partial \xi_2} - \frac{q''}{q'} \rho^* u_i^* \\ & + H_{c,u_i} + H_p + H_g + H_v, \end{aligned} \quad (2.24)$$

$$\frac{\partial \rho^* Y^*}{\partial s} + \frac{\partial \rho^* Y^* u_j^*}{\partial \xi_j} = \frac{\partial}{\partial \xi_j} \left(\rho^* D \frac{\partial Y^*}{\partial \xi_j} \right) + \left(\frac{q'}{q} \xi_2 + \frac{q_0}{q} \delta' \right) \frac{\partial \rho^* Y^*}{\partial \xi_2} + H_{c,Y} + H_{D,Y}, \quad (2.25)$$

where

$$H_{c,\phi} = \left(1 - \frac{q'}{q'_0} \right) \frac{\partial \rho^* \phi^* u_j^*}{\partial \xi_j} + \frac{q'}{q'_0} \left(1 - \frac{q_0}{q} \right) \frac{\partial \rho^* \phi^* u_2^*}{\partial \xi_2}, \quad \text{for } \phi = 1, u_i, \text{ or } Y, \quad (2.26)$$

$$H_p = \left(1 - \frac{q'_0}{q'} \right) \frac{\partial p^*}{\partial \xi_i}, \quad H_g = \left(1 - \frac{q'_0}{q'} \right) \rho^* g \delta_{2i}, \quad (2.27a,b)$$

$$H_v = \left(\frac{q_0}{q} - 1 \right) \frac{\partial \tau_{ij}^{e*}}{\partial \xi_j} + \left(\frac{q_0}{q} - 1 \right) \frac{\partial}{\partial \xi_2} \left[\tau_{i2}^* + \left(\frac{q_0}{q} - 1 \right) \tau_{i2}^{e*} \right], \quad (2.28)$$

$$H_{D,Y} = \left(\frac{q_0^2}{q^2} - 1 \right) \frac{\partial}{\partial \xi_2} \left(\rho^* D \frac{\partial Y^*}{\partial \xi_2} \right), \quad (2.29)$$

$$\tau_{ij}^* = \rho^* \nu \left(\frac{\partial u_i^*}{\partial \xi_j} + \frac{\partial u_j^*}{\partial \xi_i} - \frac{2}{3} \frac{\partial u_k^*}{\partial \xi_k} \delta_{ij} \right), \quad (2.30)$$

$$\tau_{ij}^{e*} = \rho^* \nu \left(\delta_{2j} \frac{\partial u_i^*}{\partial \xi_2} + \delta_{2i} \frac{\partial u_j^*}{\partial \xi_2} - \frac{2}{3} \frac{\partial u_2^*}{\partial \xi_2} \delta_{ij} \right). \quad (2.31)$$

Throughout this report, the * superscript will be used to distinguish a quantity that is computed in the rescaled (s, ξ) coordinates from its equivalent definition in physical (t, x) coordinates. Until this point, no simplifying assumptions have been made. Equations (2.23)–(2.25) are the rescaled NSE (RNSE) and their solution is identical to that of the NSE, as long as the appropriate transformation is applied to the resulting fields. Theoretically, the RNSE can be solved in the rescaled (s, ξ) coordinate system with $q(t) = h_i(t)$ to simulate a rescaled TRT flow with a statistically stationary height. Then, its solution can be mapped onto physical coordinates to represent a traditional TRT flow exactly. However, in a turbulent TRT flow, the range of length scales grows with time. When simulated on a fixed grid, the rescaled Kolmogorov length scale will decrease as $\eta/h \sim h^{-9/8}$ (Chertkov 2003; Ristorcelli & Clark 2004) and eventually fall below acceptable DNS resolution. There is no computational benefit to simulating the RNSE over the NSE, unless further simplifications are made.

2.2.2. Simplifying assumptions

We proceed to make the following three simplifying assumptions:

- (I) The governing equations evaluated at $\delta(t) = \delta(t_0)$ and $q(t) = q(t_0)$ are valid for a small window of time centred at $t = t_0$.
- (II) There exist functions $q(t)$ and $\delta(t)$ such that ensemble-averaged quantities are statistically stationary, i.e. $\partial \langle \cdot \rangle / \partial s = 0$.
- (III) The function $q(t)$ exhibits self-similar growth as in (1.3):

$$q'^2 = 4\alpha_q A g q. \quad (2.32)$$

For ease of reference, these assumptions are stated above as a whole, but will be mentioned individually in the following derivation as they arise. Their validity will be assessed in § 5.

Applying assumption (I), (2.23)–(2.25) are evaluated at $t = t_0$ and simplified to a set of equations that resemble the original NSE, but with additional source terms:

$$\frac{\partial \rho^*}{\partial s} + \frac{\partial \rho^* u_j^*}{\partial \xi_j} = \underbrace{\left(\frac{q'_0}{q_0} \xi_2 + \delta'_0 \right)}_{S_1} \frac{\partial \rho^*}{\partial \xi_2}, \quad (2.33)$$

$$\frac{\partial \rho^* u_i^*}{\partial s} + \frac{\partial \rho^* u_i^* u_j^*}{\partial \xi_j} = -\frac{\partial p^*}{\partial \xi_i} + \frac{\partial \tau_{ij}^*}{\partial \xi_j} - \rho^* g \delta_{2i} + \underbrace{\left(\frac{q'_0}{q_0} \xi_2 + \delta'_0 \right)}_{S_{u_i}} \frac{\partial \rho^* u_i^*}{\partial \xi_2} - \underbrace{\frac{q''_0}{q'_0} \rho^* u_i^*}_{T_i}, \quad (2.34)$$

$$\frac{\partial \rho^* Y^*}{\partial s} + \frac{\partial \rho^* Y^* u_j^*}{\partial \xi_j} = \frac{\partial}{\partial \xi_j} \left(\rho^* D \frac{\partial Y^*}{\partial \xi_j} \right) + \underbrace{\left(\frac{q'_0}{q_0} \xi_2 + \delta'_0 \right)}_{S_Y} \frac{\partial \rho^* Y^*}{\partial \xi_2}. \quad (2.35)$$

Equations (2.33)–(2.35) are the SRT equations and are no longer equivalent to the NSE; they are only assumed to be valid within a short time window centred about a specified time $t = t_0$. Section 5.3 discusses this window of validity and provides an estimate of the neglected terms. The SRT equations (in rescaled variables) resemble the full NSE (in physical variables), but with additional terms. The terms S_1 , S_{u_i} and S_Y arise from the scaling of the x_2 -coordinate and differ only in the transported quantity. They are collectively referred to as

$$S_\phi = \left(\frac{q'_0}{q_0} \xi_2 + \delta'_0 \right) \frac{\partial \rho^* \phi^*}{\partial \xi_2} = \left(\frac{1}{\tau_0} \xi_2 + \delta'_0 \right) \frac{\partial \rho^* \phi^*}{\partial \xi_2}, \quad (2.36)$$

where $\phi = 1, u_i, Y$ for continuity, momentum and scalar transport equations, respectively. In addition, a time scale, $\tau_0 = q_0/q'_0$, is introduced for notational simplicity. In the momentum equation, T_i arises from velocity scaling. Using assumption (III), (2.32) can be differentiated in time and divided by $2q'^2$ to yield $q''/q' = 2\alpha_q A g/q' = q'/(2q)$. Hence,

$$T_i = -\frac{q''_0}{q'_0} \rho^* u_i^* = -\frac{1}{2} \frac{q'_0}{q_0} \rho^* u_i^* = -\frac{1}{2\tau_0} \rho^* u_i^*. \quad (2.37)$$

Based on (2.36) and (2.37), the SRT equations, (2.33)–(2.35), require the specification of two additional parameters: a time scale τ_0 , and a velocity δ'_0 .

2.2.3. Boundary conditions

Applying the coordinate transformation, (2.20) and (2.21), to (2.8)–(2.10), the boundary conditions in the transformed coordinate system are

$$\mathbf{u}^*(\xi_2 \rightarrow \pm\infty) = 0, \quad (2.38)$$

$$\rho^*(\xi_2 \rightarrow -\infty) = \rho_L, \quad \rho^*(\xi_2 \rightarrow \infty) = \rho_H, \quad (2.39a,b)$$

$$Y^*(\xi_2 \rightarrow -\infty) = 0, \quad Y^*(\xi_2 \rightarrow \infty) = 1. \quad (2.40a,b)$$

In short, the boundary conditions are fully consistent between TRT and SRT configurations.

2.3. Stationary solution

Until now, assumption (II) has not been used. In this section, we assume the existence of a stationary state, and establish how τ_0 and δ'_0 are related to the stationary flow solution. The same integral flow quantities defined in § 2.1.3 are considered here using the SRT equations, and their stationary solutions are presented.

2.3.1. Displacement length

The time evolution of the displacement length (in rescaled variables)

$$\delta_I^*(s) = \frac{1}{\rho_H - \rho_L} \left(\int_0^{+\infty} (\rho_H - \langle \rho^* \rangle) d\xi_2 + \int_{-\infty}^0 (\rho_L - \langle \rho^* \rangle) d\xi_2 \right), \quad (2.41)$$

is derived in the same way as (2.14). Like $\delta_I(t)$, $\delta_I^*(s)$ is a displacement length that quantifies the location of the mixing layer with respect to $\xi_2 = 0$. The ensemble average of (2.33) is

$$\frac{\partial \langle \rho^* \rangle}{\partial s} + \frac{\partial \langle \rho^* u_2^* \rangle}{\partial \xi_2} = \frac{1}{\tau_0} \xi_2 \frac{\partial \langle \rho^* \rangle}{\partial \xi_2} + \delta'_0 \frac{\partial \langle \rho^* \rangle}{\partial \xi_2}. \quad (2.42)$$

We integrate (2.42) in two parts and sum them to get

$$\frac{d\delta_I^*}{ds} = -\frac{1}{\tau_0} \delta_I^* - \delta'_0. \quad (2.43)$$

Assuming the existence of a stationary state, $d\delta_I^*/ds = 0$, and

$$\delta'_0 = -\frac{1}{\tau_0} \delta_I^*. \quad (2.44)$$

Equation (2.44) shows that the displacement length in the stationary state is controlled by both δ'_0 and τ_0 . To decouple them, we consider a second integral quantity, the mixing height.

2.3.2. Mixing height

A transport equation for the mixing height

$$h_m^*(s) = \frac{4}{\rho_0} \int_{-\infty}^{+\infty} \langle \rho^* m^* \rangle d\xi_2, \quad m^* = Y^*(1 - Y^*), \quad (2.45)$$

is derived from the SRT equations following the same procedure outlined in the derivation of (2.17). The ensemble-averaged transport equation for the local mixed mass is

$$\frac{\partial \langle \rho^* m^* \rangle}{\partial s} = -\frac{\partial \langle \rho^* m^* u_2^* \rangle}{\partial \xi_2} + \frac{\partial}{\partial \xi_2} \left\langle \rho^* D \frac{\partial m^*}{\partial \xi_2} \right\rangle + \langle \rho^* \chi^* \rangle + \left(\frac{1}{\tau_0} \xi_2 + \delta'_0 \right) \frac{\partial \langle \rho^* m^* \rangle}{\partial \xi_2}, \quad (2.46)$$

where $\chi^* = 2D(\partial Y^*/\partial \xi_j)^2$. Integrating over ξ_2 results in

$$\frac{dh_m^*}{ds} = \frac{4}{\rho_0} \Phi_\chi^* - \frac{1}{\tau_0} h_m^*, \quad (2.47)$$

where $\Phi_\chi^*(s) = \int_{-\infty}^{+\infty} \langle \rho^* \chi^* \rangle d\xi_2$. In a stationary state, $dh_m^*/ds = 0$, and

$$\frac{1}{\tau_0} = \frac{4\Phi_\chi^*}{\rho_0 h_m^*}. \quad (2.48)$$

Hence, (2.48) and (2.44) form a set of two equations that relates the parameters τ_0 and δ_0' with the displacement length δ_I^* and mixing height h_m^* of the SRT flow.

2.3.3. Relationship to temporal Rayleigh–Taylor flow

Based on assumptions (I) and (II) in § 2.2.2, the SRT equations are solved for a statistically stationary flow that is statistically equivalent to self-similar TRT flow at $t = t_0$. When $t = t_0$, the transformations in (2.20) and (2.21) reduce to $\mathbf{u}^* = \mathbf{u}$ and $\xi = x$. For these two reasons, any ensemble-averaged SRT quantity $\Omega^*(\xi, \mathbf{u}^*)$ is expected to be equal to its TRT equivalent $\Omega(x, \mathbf{u})$ when evaluated at $t = t_0$, i.e.

$$\Omega^*(\xi, \mathbf{u}^*) = \Omega(x, \mathbf{u}, t = t_0). \quad (2.49)$$

The TRT definitions introduced in § 2.1.3 are revisited, but evaluated only at $t = t_0$. Equation (2.18) is evaluated at $t = t_0$, related to SRT using (2.49), and compared with (2.48) to yield

$$\frac{1}{h_m} \frac{dh_m}{dt} \Big|_{t=t_0} = \frac{4\Phi_\chi}{\rho_0 h_m} \Big|_{t=t_0} = \frac{4\Phi_\chi^*}{\rho_0 h_m^*} = \frac{1}{\tau_0}. \quad (2.50)$$

Hence, the SRT parameter τ_0 corresponds to the time scale that governs the growth of h_m of a TRT layer at $t = t_0$.

In TRT flow, δ_I is constant due to the physical boundary conditions. In SRT flow, δ_I^* is constant by virtue of stationarity. Applying (2.49) to δ_I and substituting (2.44), we get

$$\delta_I(t = t_0) = \delta_I(t = 0) = \delta_I^* = -\tau_0 \delta_0'. \quad (2.51)$$

Together with τ_0 , δ_0' contains information about the initial position of the interface for the equivalent TRT flow. The SRT parameter δ_0' simply shifts the mixing layer. Because the dynamics of a TRT flow is not affected by a spatial shift, δ_0' has no impact on the flow dynamics.

3. Statistically stationary Rayleigh–Taylor flow inputs

The complete SRT equations are defined by (2.33)–(2.35) and require the specification of two parameters, τ_0 and δ_0' . After a statistically stationary state has been reached, we expect (2.44) and (2.48) to be satisfied. There are multiple ways to reach this stationary state through the choice of implementation of τ_0 and δ_0' ; a comprehensive discussion of possible approaches is presented in Appendix A. In this study, τ_0 and δ_0' are not prescribed as constant inputs, but vary in time through closure equations with constant inputs \bar{h}_m and $\bar{\delta}_I$. A brief description of this procedure is presented below.

3.1. Implementation of τ_0 and δ'_0

A constant mixing width, $\bar{h}_m > 0$, is prescribed as an input to the stationarity relation (2.48) such that $\tau_0(s)$ is continuously updated as

$$\frac{1}{\tau_0(s)} = \frac{4\Phi_\chi^*(s)}{\rho_0 \bar{h}_m}. \quad (3.1)$$

Substituting (3.1) into (2.47) gives

$$\frac{dh_m^*}{ds} = \frac{4\Phi_\chi^*}{\rho_0} \left(1 - \frac{h_m^*}{\bar{h}_m} \right). \quad (3.2)$$

Both Φ_χ^* and h_m^* are positive by definition. This guarantees the relaxation of the instantaneous layer width to the prescribed target value, $h_m^*(s) \rightarrow \bar{h}_m$, regardless of its initial value. The stationary value of h_m^* is determined solely by the choice of \bar{h}_m .

Analogously, a constant input value for the displacement length, $\bar{\delta}_I$, is used as an input to (2.44), so that $\delta'_0(s)$ is continuously updated as

$$\delta'_0(s) = -\frac{1}{\tau_0(s)} \bar{\delta}_I. \quad (3.3)$$

Equation (2.43) becomes

$$\frac{d\delta_I^*}{ds} = \frac{1}{\tau_0} (\bar{\delta}_I - \delta_I^*). \quad (3.4)$$

Because $1/\tau_0 > 0$, (3.4) is a stable equation. $\delta_I^*(s)$ relaxes toward a prescribed value $\bar{\delta}_I$ that serves as a known reference location at all times once the flow has converged to stationarity. The stationary value of δ_I^* is determined completely by the user input $\bar{\delta}_I$.

3.2. Independent non-dimensional inputs

The evolution of SRT flow is governed by (2.33)–(2.35) and the two closure equations (3.1) and (3.3). The SRT equations require the specification of gravity (g) and fluid properties (ρ_H, ρ_L, v, D), while the closure equations require inputs \bar{h}_m and $\bar{\delta}_I$. Although practically prescribed as an input, $\bar{\delta}_I$ is not considered a physical input parameter because it simply shifts the mixing layer and has no dynamical impact.

Additionally, because the SRT equations are solved on a finite domain over long simulation times, there are two key differences in flow inputs between SRT and TRT flow. First, domain dimensions may exert an influence on SRT flow physics. As the large flow length scales grow laterally and approach the size of the domain, the lateral domain width, $\mathcal{L} = \mathcal{L}_1 = \mathcal{L}_3$, may impact the flow physics. Thus, \mathcal{L} is considered an independent input parameter. The vertical domain height is simply chosen to be much larger than \bar{h}_m , such that it has no effect on the flow. Second, while the initial conditions to the SRT simulation (at $s = 0$) can generally be considered an input, it is assumed that the long-time nature of SRT flow leads to a stationary solution that is independent of initial conditions. This is verified in § 5.2.

Applying the Buckingham Pi theorem on seven independent variables ($g, \rho_H, \rho_L, v, D, \bar{h}_m, \mathcal{L}$) and three dimensions (mass, length, time), the flow can be fully defined by four

non-dimensional numbers:

$$A = \frac{\rho_H - \rho_L}{\rho_H + \rho_L}, \quad Sc = \frac{\nu}{D}, \quad Gr = \frac{Ag\bar{h}_m^3}{\nu^2}, \quad \lambda = \frac{\bar{h}_m}{\mathcal{L}}, \quad (3.5a-d)$$

where A is the Atwood number, Sc the Schmidt number, Gr the Grashof number and λ the aspect ratio of the mixing layer.

The values of A and Sc are determined entirely by fluid properties. The Grashof number Gr approximates the ratio of the large-scale buoyancy forces to the small-scale viscous forces, reflecting the extent of scale separation and turbulence intensity in the flow. While Gr is the input to SRT flow, turbulence intensity is commonly represented in the TRT literature by the Reynolds number, which is an output parameter for both SRT and TRT flow. For a self-similar TRT flow, Gr scales monotonically with Re^2 . This can be shown by invoking $\bar{h}_m \approx h_m^* = h_m(t_0)$, substituting (1.3) and assuming the proportionality of large length scales in self-similar flows, i.e.

$$Gr = \frac{Ag\bar{h}_m^3}{\nu^2} \approx \frac{Agh_m^3}{\nu^2} \propto \frac{h_m^2 \dot{h}_m^2}{\nu^2} \propto \left(\frac{H\dot{H}}{\nu} \right)^2 = Re^2. \quad (3.6)$$

For SRT flow, the Reynolds number is defined as

$$Re^* = \frac{H^{*2}}{\tau_0 \nu}, \quad (3.7)$$

which is derived by evaluating (1.4) at $t = t_0$ and relating H to τ_0 using (2.19) and (2.50). Because Re is more commonly used in the TRT literature, comparisons with TRT flow will be presented in terms of Re . Finally, \bar{h}_m and \mathcal{L} constrain the growth of large-scale structures in the vertical and horizontal directions, respectively. Hence, λ may affect the size and distribution of flow structures generated in the SRT configuration.

4. Numerical method and simulation cases

4.1. Numerical method

Simulations are performed using the computational solver, NGA (Desjardins *et al.* 2008). The numerical code solves the conservative-variable formulation of the low-Mach-number NSE with staggered finite difference operators and uses a fractional step method to enforce continuity. The NSE are solved using a second-order semi-implicit iterative midpoint scheme and uses staggering in time between the momentum field and the scalar and density fields. The scalar is advanced first, the density field is updated and the momentum equations are then advanced. The resulting computational framework conserves kinetic energy discretely (i.e. there is no numerical viscosity). While high order of accuracy is available in NGA for the continuity and momentum equations, second-order discretization is selected for the present simulations. The combination of spatial staggering, discrete energy conservation and resolution of the Kolmogorov scales was found to be more important than the order of accuracy in reproducing key statistics (including energy spectra) in DNS of homogeneous isotropic turbulence (Desjardins *et al.* 2008).

The bounded cubic Hermite polynomial (BCH) (Verma, Xuan & Blanquart 2014) scheme is used for scalar transport. The BCH scheme was chosen because it ensures scalar boundedness and has less numerical diffusion than other schemes, including weighted essentially non-oscillatory schemes. In particular, Verma *et al.* (2014) found that other bounded schemes require at least twice the spatial resolution to resolve small-scale scalar

features as well as BCH. A Courant–Friedrichs–Lewy condition of $\text{CFL} \leq 0.8$ is imposed for all simulations in the current study. Details on the implementation of the primitive NSE and scalar transport can be found in the original publications. Only the implementation of the additional SRT terms S_ϕ and T_i is addressed below.

The additional terms in the SRT equations include two parameters τ_0 and δ'_0 , which are not prescribed as constants but as functions of the evolving flow, $\tau_0(Y^*(s, \xi), \bar{h}_m)$ and $\delta'_0(\tau_0(s), \bar{\delta}_I)$. They are updated once every timestep using (3.1) and (3.3), respectively. The S_ϕ terms, defined in (2.36), are computed using the analytically equivalent expression

$$S_\phi = \underbrace{\frac{\partial \rho^* v_s \phi^*}{\partial \xi_2}}_{S_{\phi,f}} - \underbrace{\frac{1}{\tau_0} \rho^* \phi^*}_{S_{\phi,b}}, \quad (4.1)$$

where $v_s = (\xi_2/\tau_0 + \delta'_0)$ can be treated as a contribution to the convective velocity from S_ϕ . The first term $S_{\phi,f}$ is implemented by applying a pointwise correction of $-v_s$ to the u_2^* term in the convective term of the respective governing equation. By using the form shown in (4.1), the implementation of $S_{\phi,f}$ leverages the stable semi-implicit schemes already developed within NGA. The second term $S_{\phi,b}$ is implemented pointwise, as is T_i from the momentum equation. Both terms are stabilizing and have much larger relaxation time scales than the simulation timestep – they are expected to be numerically stable. Nonetheless, they are implemented using a semi-implicit treatment to ensure consistency across all terms.

4.2. Simulation cases

Simulations are performed on a three-dimensional rectangular domain. The top and bottom boundaries are implemented as Dirichlet boundary conditions and the lateral boundaries as periodic. All simulations are performed at $A = 0.5$ and $Sc = 1$ with constant ν and D to enable direct comparisons with the DNS results of Cabot & Cook (2006).

The computational grid is centred at the origin with domain lengths \mathcal{L}_i and grid spacing Δ_i . In the horizontal directions, $\mathcal{L}_1 = \mathcal{L}_3 = \mathcal{L}$, and $\Delta_1 = \Delta_3 = \mathcal{L}/N_1$, where $N_1 = N_3$ is the number of grid points in each direction. In all simulations, $\mathcal{L} = 1$ is fixed. In the vertical direction, Δ_2 varies with ξ_2 . A uniformly spaced ($\Delta_2 = \Delta_1$) core grid of length $\mathcal{L}_{2c} = N_{2c} \Delta_1$ is used to resolve the bulk of the mixing layer ($|\xi_2| \leq \mathcal{L}_{2c}/2$). This core grid region is defined to be 10 % wider than the region that contains the 1 % and 99 % mean mole fraction locations. Outside the core (where $|\xi_2| > \mathcal{L}_{2c}/2$), the vertical spacing $\Delta_2(\xi_2)$ is stretched with a factor of 1.1. The total domain height satisfies the condition $\mathcal{L}_2 > 4\mathcal{L}_{2c}$. Additionally, $\bar{\delta}_I$ is used to shift the mixing layer so that it lies within the refined core grid. In the vertical direction, the results were verified to be insensitive to a larger domain or core grid region.

A list of the simulation cases conducted is summarized in table 3 (with more detailed parameters provided in Appendix B). Case T0 simulates the temporal growth of an RT mixing layer using the primitive NSE from an initially perturbed planar interface. Following a similar procedure to Cook *et al.* (2004), the mass fraction is initialized as

$$Y(\mathbf{x}) = \frac{1}{2} \left[1 + \text{erf} \left(\frac{x_2}{\delta_t} + \psi(x_1, x_3) \right) \right], \quad (4.2)$$

where the initial thickness of the interface is $\delta_t = 0.0025\mathcal{L}$ and $\psi(x_1, x_3)$ is a field of random isotropic perturbations with a Gaussian spectrum centred at $\kappa_0 = 64\pi/\mathcal{L}$

Case	Initial condition	Inputs				$(\kappa_{\max}\eta^*)_{\min}$	
		$Gr(\times 10^6)$	λ	$\bar{\delta}_I/\bar{h}_m$	N_1		
T0	Planar interface	$\lesssim 39.3$	—	—	1024	954	$\gtrsim 3.04$
I1/K2/L3/G4	TRT	7.39	1.5	0.119	128	456	2.99
I2	Planar interface	7.39	1.5	0.119	128	456	2.97
I3	G3	7.39	1.5	0.119	128	456	2.98
K1	K2	7.39	1.5	0.119	64	228	1.51
K3	K2	7.39	1.5	0.119	256	910	5.94
L1	TRT	7.39	0.5	0.163	384	624	3.06
L2	TRT	7.39	1.0	0.128	192	490	2.95
L4	TRT	7.39	2.0	0.115	96	440	3.10
L5	TRT	7.39	2.5	0.113	78	440	3.25
G1	Planar interface	0.183	1.5	0.119	32	114	2.83
G2	G1	1.16	1.5	0.119	64	228	2.91
G3	G2	3.43	1.5	0.119	96	342	2.94
G5	G4	46.9	1.5	0.119	256	910	3.04
G6	G5	138	1.5	0.119	384	1364	3.07

Table 3. List of simulation cases.

and standard deviation $\sigma_\kappa = \kappa_0/6$. The perturbation field is normalized so that its root-mean-square value is $\psi_{rms} = 0.01$. Based on the results from Cabot & Cook (2006), both the growth and mixedness parameters seem to settle into their self-similar values by $Re = HH/v \approx 2000$. Separately, the flow may experience lateral confinement effects as the layer height approaches the lateral domain length (Dalziel *et al.* 2008; Boffetta *et al.* 2012a). To minimize these effects, we apply an upper limit of $H(t)/\mathcal{L} \approx 0.72$, which is deduced from the final simulation time of Cabot & Cook (2006) (details are shown in Appendix C). Viscosity and grid parameters are chosen to ensure that a sufficient range of $Re(t) \geq 2000$ is well resolved within these $H(t)$ limits. Case T0 serves three objectives. First, we validate our numerical framework against other TRT results found in the literature. Second, the self-similar scaling assumption of the SRT equations is verified. Third, T0 is used as a basis for detailed comparisons with subsequent SRT simulations, which differ only in their mathematical framework but maintain consistency in numerical methods, grid resolution, normalizations and flow conditions.

In the remaining cases, the SRT equations are solved. Each of these cases is labelled with a prefix representing the parameter that is varied, i.e. ‘I’ for initial condition, ‘K’ for $\kappa_{\max}\eta^*$, ‘L’ for aspect ratio λ and ‘G’ for Grashof number. With the exception of ‘I’ cases, the accompanying number scales with the magnitude of the parameter being studied. Case I1/K2/L3/G4 has multiple labels because it is a part of multiple parametric studies.

The effect of initial conditions on SRT flow is studied using I1–I3. Case I1 is first evolved as a TRT flow from the initial conditions stated in (4.2) with the same perturbation spectrum and initial thickness. Once the target height is reached, the SRT equations are solved. Case I2 is initialized as (4.2) and evolves entirely via the SRT equations. Finally, I3 is initialized by interpolating a fully developed statistically stationary snapshot from G3, an SRT flow of the same height but smaller Grashof number.

Different grid resolutions are considered to examine the effect of numerical errors on the simulation results. Grid resolution is quantified using $\kappa_{\max}\eta^*$, where $\kappa_{\max}(\xi_2) = \pi/\Delta_2(\xi_2)$

is the maximum resolved wavenumber, and η^* is the Kolmogorov scale, estimated as

$$\eta^*(\xi_2) = \left[\frac{\langle \rho^* \rangle v^3}{\langle \rho^* \epsilon^* \rangle} \right]^{1/4}, \quad \langle \rho^* \epsilon^* \rangle = \left\langle \tau_{ij}^* \frac{\partial u_i^*}{\partial \xi_j} \right\rangle. \quad (4.3)$$

In SRT flow, $\kappa_{max}\eta^*$ varies with ξ_2 , and [table 3](#) provides the minimum values. Grid resolution effects are studied for $1.5 \lesssim \kappa_{max}\eta^* \lesssim 6.0$ using K1–K3 and reported in [Appendix D](#). In summary, $\kappa_{max}\eta^* \approx 3$ is deemed sufficient, and is used as a target spatial resolution for all cases. This resolution is also similar to the final time of Cabot & Cook ([2006](#)).

The final two sets of simulations address the effects of the physical input parameters identified in [§ 3.2](#). As discussed, A and Sc are not varied. The effect of the mixing layer aspect ratio is studied at constant Gr using simulations L1–L5, corresponding to $0.5 \leq \lambda \leq 2.5$. Lastly, the effect of Grashof number is studied at constant $\lambda = 1.5$ using simulations G1–G6, for Grashof numbers up to $Gr = 1.39 \times 10^8$.

5. Results: analysis of SRT framework

In this section, we verify large-scale self-similarity in TRT flow, demonstrate the convergence of SRT flows to stationarity and validate the simplifying assumptions used to derive the SRT equations. The effect of different physical inputs on SRT flow will be studied in [§ 6](#). Throughout §§ 5 and 6, comparisons will be made with Cabot & Cook ([2006](#)) and subsequent analysis of the same dataset (Livescu *et al.* [2009](#); Chung & Pullin [2010](#); Zhou & Cabot [2019](#)), which may be referred to as the ‘reference’ TRT dataset.

5.1. Temporally growing Rayleigh–Taylor mixing layer

The results from TRT simulation T0 are presented here. In [§ 5.1.1](#), different growth regimes of T0 are identified. In [§ 5.1.2](#), the data from the self-similar phase are used to validate the scaling assumptions of the SRT equations.

5.1.1. Self-similar growth in TRT

Since TRT flow is non-stationary and homogeneous in the horizontal directions, it is customary to estimate ensemble averages with planar averages, i.e. $\langle \cdot \rangle(t, x_2) = \langle \cdot \rangle_{1,3}(t, x_2)$. However, this may result in profiles with significant statistical noise. To mitigate this issue, we leverage self-similar scaling and average results over a small time window, $t_1 < t < t_2$. Specifically, dimensional data are averaged first in the horizontal directions, then normalized using self-similar scaling, and finally averaged over a small time window. For example, the ensemble-averaged normalized kinetic energy is computed as

$$\left[\frac{\langle \rho u_i^2 / 2 \rangle}{\rho_0 A g h_p} \right]_{TRT} \left(t, \frac{x_2 - \delta_I}{h_p} \right) = \left\langle \frac{\langle \rho u_i^2 / 2 \rangle_{1,3}(t, (x_2 - \delta_I) / h_p(t))}{\rho_0 A g h_p(t)} \right\rangle_{t_1 \leq t \leq t_2}. \quad (5.1)$$

The assumed scaling is only valid if the flow is indeed self-similar. In the general case, a small time window is used simply to reduce statistical noise. However, in the self-similar growth regime, larger time windows can be used.

Case T0 is initialized as a perturbed planar interface, and its mathematical description is detailed in [§ 4.2](#). Large wavenumber perturbations ($\ell_I \ll h(t)$) are chosen to encourage

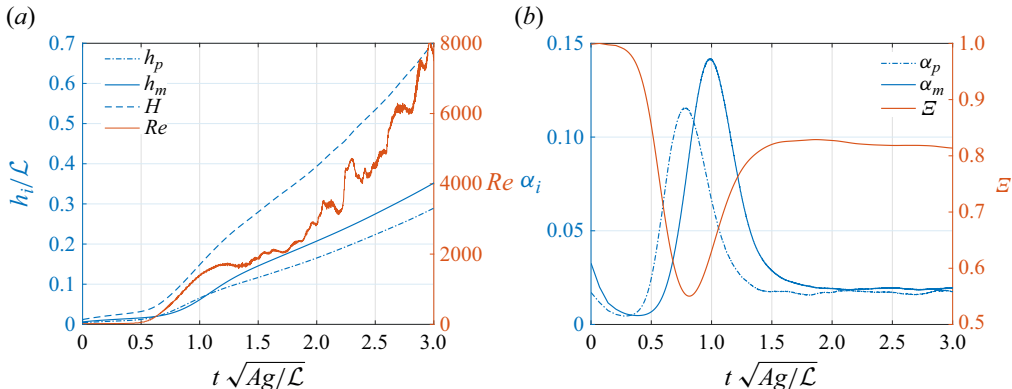


Figure 1. Temporal evolution for TRT-T0: (a) normalized heights and Reynolds number; (b) growth and mixedness parameters. Height definitions are summarized in table 1.

late-time self-similar growth that is driven by mode-coupling processes. The time evolution of several quantities derived from the density field is shown in figure 1. Because there is no constant characteristic time scale in TRT, time is non-dimensionalized by $(\mathcal{L}/Ag)^{1/2}$, an arbitrary choice of no physical significance. In figure 1(a), the mixing layer growth is represented by three different height definitions (defined in table 1): h_p is the product height that will be used for comparisons with Cabot & Cook (2006); h_m is the mixing height that will be used as an input parameter to the SRT equations; and H is a threshold-based height.

To minimize domain confinement effects, simulations were stopped shortly after $H(t)/\mathcal{L} > 0.7$. The height $H(t)$ is also used to compute the Reynolds number, $Re = H\dot{H}/\nu$. Because H is determined from averages over a plane, it is more susceptible to noise than integral height definitions like h_p or h_m . Its time derivative \dot{H} is computed using a second-order finite difference in time, which exacerbates statistical noise and contributes to significant fluctuations in Re . Nonetheless, a growing Reynolds number is clearly observed. The largest Re considered in this simulation, attained at $t(Ag/\mathcal{L})^{1/2} = 3$, is approximately 8000.

The integral heights h_p and h_m from figure 1(a) are normalized using self-similar scaling (1.3) to obtain the growth parameters, $\alpha_i = \dot{h}_i^2/(4Agh_i)$, shown in figure 1(b). The mixedness parameter Ξ is defined identically to Cabot & Cook (2006) as

$$\Xi = \frac{1}{h_p} \int_{-\infty}^{\infty} 2\langle \min(X, 1-X) \rangle \, dx_2. \quad (5.2)$$

A diffusion-dominated regime is observed for $t(Ag/\mathcal{L})^{1/2} \lesssim 0.2$, where the flow is almost fully mixed at $\Xi \approx 1$ and the growth parameter decreases. Subsequently, RT instabilities cause large-amplitude changes in all parameters before the flow transitions to turbulence and reaches quadratic self-similar growth at $t(Ag/\mathcal{L})^{1/2} \geq 2$. While more sophisticated data analysis techniques can be used to quantify the extent of flow self-similarity (Morgan *et al.* 2017), the self-similar phase in T0 is identified visually by the stationary behaviour of key statistical parameters. This onset of self-similar growth happens at $Re \approx 3000$. Although $Re \approx 2000$ was identified in § 4.2 as a lower bound for observed self-similarity in Cabot & Cook (2006), figure 1(b) shows that this is true for

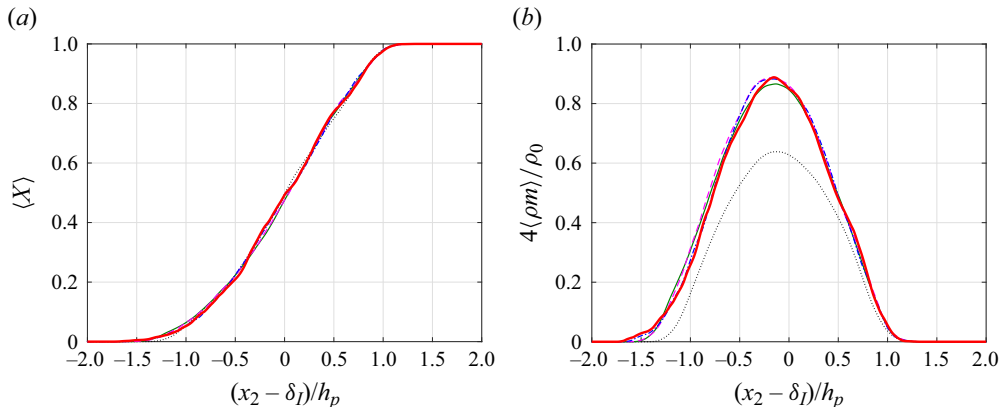


Figure 2. Temporal evolution for TRT-T0: (a) heavy fluid mole fraction; (b) normalized local mixed mass. Lines represent $t(Ag/\mathcal{L})^{1/2} = 1.0$ (black dotted), 1.5 (green solid), 2.0 (magenta dashed), 2.5 (blue dash-dotted), 3.0 (red thick solid), corresponding to $Re \approx 1400, 1900, 2800, 4400$, and 8000, respectively. One-dimensional profiles are first normalized, then averaged over $t(Ag/\mathcal{L})^{1/2} \pm 0.1$ to reduce statistical variability.

α_p , but not for α_m . Indeed, it is well known that not all statistics in TRT flow achieve self-similar behaviour at the same time. Figure 2 shows one-dimensional scalar statistics and further illustrates this: in figure 2(a), the average mole fraction $\langle X \rangle$ appears to be converged by $t(Ag/\mathcal{L})^{1/2} = 1$, while the local mixed mass in figure 2(b) only converges around $t(Ag/\mathcal{L})^{1/2} = 1.5$.

For the purposes of comparison with Cabot & Cook (2006) and subsequent SRT results, $2 \leq t(Ag/\mathcal{L})^{1/2} \leq 3$ is taken as the time window where the scalar field exhibits self-similarity. Time averages are calculated over this window to yield $\alpha_m = 0.0190$, $\alpha_p = 0.0173$ and $\mathcal{E} = 0.814$. Values of α_p and \mathcal{E} were extracted from figures 4 and 6 of Cabot & Cook (2006) and averaged over time for $Re > 3000$. These values, $\alpha_p \approx 0.019$ and $\mathcal{E} \approx 0.82$, compare well with those obtained from case T0.

Next, the velocity statistics of T0 are examined. Figure 3(a) shows the time evolution of vertically integrated kinetic energy, $K = \int_{-\infty}^{+\infty} \langle \rho k \rangle dx_2$, where $k = u_i u_i / 2$, while figure 3(b) shows the planar-averaged profiles. Figure 3(a) illustrates that the normalized total kinetic energy has a small positive slope for $t(Ag/\mathcal{L})^{1/2} \geq 2$, indicating that the velocity statistics of T0 may not be fully self-similar, despite stationarity in α_i values. This faster-than-self-similar growth is also observed in the normalized one-dimensional profiles shown in figure 3(b), where the magnitudes continue to increase (albeit slowly) for $t(Ag/\mathcal{L})^{1/2} \geq 2$.

Although T0 does not demonstrate true self-similarity in velocity, the onset of slow growth in normalized kinetic energy aligns with the time window for scalar self-similarity. Hence, the same time window, $2 \leq t(Ag/\mathcal{L})^{1/2} \leq 3$, is used to compute approximately self-similar velocity statistics for subsequent comparisons. Convergence to self-similarity in TRT is a complex issue that depends on the initial conditions and the specific flow statistic considered. It is beyond the scope of this paper to question the existence of true velocity self-similarity in TRT flow. We simply note that T0 exhibits faster-than-self-similar growth in velocity statistics for $2 \leq t(Ag/\mathcal{L})^{1/2} \leq 3$ and bear this result in mind through subsequent sections.

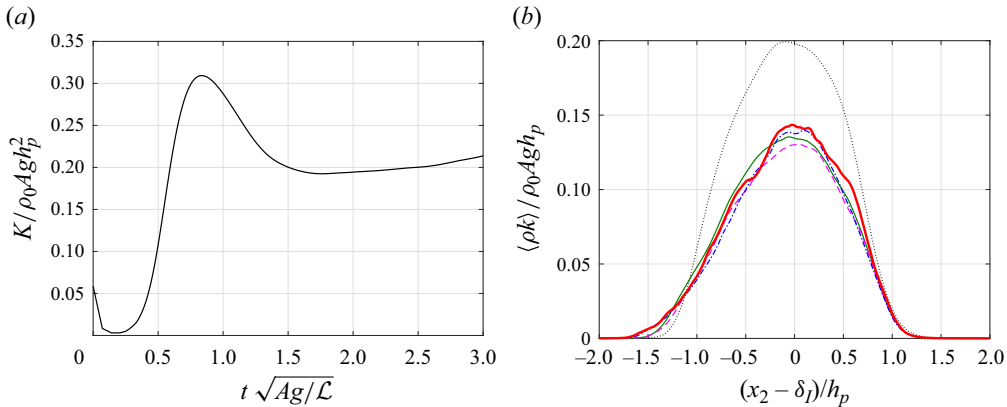


Figure 3. Temporal evolution of normalized kinetic energy for TRT-T0: (a) vertically integrated; (b) planar averaged. Lines represent $t(Ag/\mathcal{L})^{1/2} = 1.0$ (black dotted), 1.5 (green solid), 2.0 (magenta dashed), 2.5 (blue dash-dotted), 3.0 (red thick solid), corresponding to $Re \approx 1400, 1900, 2800, 4400$ and 8000, respectively. One-dimensional profiles are first normalized, then averaged over $t(Ag/\mathcal{L})^{1/2} \pm 0.1$ to reduce statistical variability.

5.1.2. *A priori* verification of SRT equations using TRT data

An important objective of the SRT flow configuration is to reproduce TRT flow dynamics. Although the derivation of the SRT equations is informed fundamentally by observations of self-similarity in TRT flow, the statistical equivalence of SRT and TRT flow, stated mathematically as (2.49), has not been demonstrated. Contrary to TRT flow, the time derivative of any ensemble-averaged quantity in a converged SRT flow is zero and is instead replaced by contributions from S_ϕ and T_i . For (2.49) to hold, the additional SRT terms must, on average, be exactly the negative of the time derivative in TRT flow. We derive the analytical mixed mass and kinetic energy budgets for SRT, assume the validity of (2.49) by evaluating the budget terms from T0 data, and verify that the contributions from S_ϕ and T_i can indeed mimic the time derivative.

In the stationary state, the balance of local mixed mass for SRT can be obtained from (2.46) by setting the time derivative to zero. This is written as

$$0 = -\frac{\partial \langle \rho^* m^* u_2^* \rangle}{\partial \xi_2} + \frac{\partial}{\partial \xi_2} \left\langle \rho^* D \frac{\partial m^*}{\partial \xi_2} \right\rangle + \langle \rho^* \chi^* \rangle + \left(\frac{1}{\tau_0} \xi_2 + \delta'_0 \right) \frac{\partial \langle \rho^* m^* \rangle}{\partial \xi_2}. \quad (5.3)$$

We assume relationship (2.49) and express (5.3) using TRT quantities, leading to

$$0 = \left[-\frac{\partial \langle \rho m u_2 \rangle}{\partial x_2} + \frac{\partial}{\partial x_2} \left\langle \rho D \frac{\partial m}{\partial x_2} \right\rangle + \langle \rho \chi \rangle \right]_{t=t_0} + \left[\frac{1}{\tau_0} (x_2 - \delta_I) \frac{\partial \langle \rho m \rangle}{\partial x_2} \right]_{t=t_0}. \quad (5.4)$$

The first three terms of (5.4) are precisely the right-hand side of the TRT mixed mass budget shown in (2.17). Their sum is exactly the time derivative of $\langle \rho m \rangle$. The final term in (5.4) is simplified using relations for τ_0 and δ'_0 from (2.50) and (2.51). Hence

$$\left[\frac{\partial \langle \rho m \rangle}{\partial t} \right]_{t=t_0} = - \left[\frac{\dot{h}_m}{h_m} (x_2 - \delta_I) \frac{\partial \langle \rho m \rangle}{\partial x_2} \right]_{t=t_0}. \quad (5.5)$$

The SRT term S_ϕ contributes a mixed mass transport term that is exactly the negative of the TRT time derivative at $t = t_0$. Both terms of (5.5) are computed from T0 data over the self-similar region, normalized by $\rho_0 (Ag/h_p)^{1/2}$, and shown in figure 4(a).

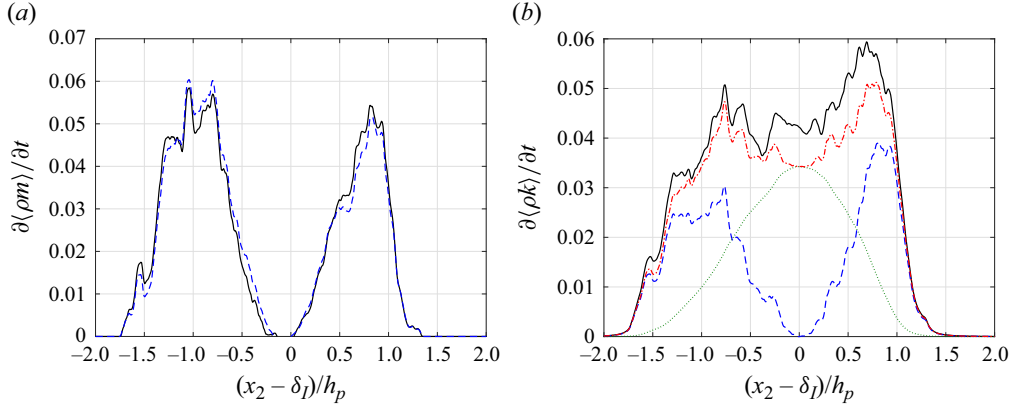


Figure 4. Verification of SRT scaling assumptions using TRT-T0 data, normalized and averaged over $2.0 \leq t(Ag/\mathcal{L})^{1/2} \leq 3.0$. Left-hand side and right-hand side terms from (5.5) and (5.8) are compared. (a) Mixed mass: time derivative (black solid); right-hand side of (5.5) (blue dashed). (b) Kinetic energy: time derivative, T (black solid); T_S (blue dashed); T_T (green dotted); $T_S + T_T$ (red dash-dotted).

The comparison in figure 4(a) shows that the right-hand side of (5.5) recovers the time derivative of the mixed mass convincingly.

The same analysis is applied to the kinetic energy budget, which includes contributions from both S_ϕ and T_i . The TRT kinetic energy budget is derived by multiplying (2.2) by u_i and invoking continuity to yield

$$\frac{\partial(\rho k)}{\partial t} = -\frac{\partial\langle\rho k u_2\rangle}{\partial x_2} - \left\langle u_i \frac{\partial p}{\partial x_i} \right\rangle + \frac{\partial\langle u_i \tau_{i2} \rangle}{\partial x_2} - \left\langle \tau_{ij}^* \frac{\partial u_i}{\partial x_j} \right\rangle - \langle \rho u_2 \rangle g. \quad (5.6)$$

The kinetic energy balance for converged SRT flow can be derived similarly by multiplying (2.34) with u_i^* , and setting the time derivative to zero. This results in

$$0 = -\frac{\partial\langle\rho^* k^* u_2^*\rangle}{\partial \xi_2} - \left\langle u_i^* \frac{\partial p^*}{\partial \xi_i} \right\rangle + \frac{\partial\langle u_i^* \tau_{i2}^* \rangle}{\partial \xi_2} - \left\langle \tau_{ij}^* \frac{\partial u_i^*}{\partial \xi_j} \right\rangle - \langle \rho^* u_2^* \rangle g + \left(\frac{1}{\tau_0} \xi_2 + \delta'_0 \right) \frac{\partial\langle\rho^* k^*\rangle}{\partial \xi_2} - \frac{1}{\tau_0} \langle \rho^* k^* \rangle, \quad (5.7)$$

where $k^* = u_i^* u_i^*/2$. After applying assumption (2.49) on (5.7) and substituting (5.6), we get

$$\underbrace{\left[\frac{\partial\langle\rho k\rangle}{\partial t} \right]_{t=t_0}}_{T(t_0)} = \underbrace{\left[-\frac{\dot{h}_m}{h_m} (x_2 - \delta_I) \frac{\partial\langle\rho k\rangle}{\partial x_2} \right]_{t=t_0}}_{T_S(t_0)} + \underbrace{\left[\frac{\dot{h}_m}{h_m} \langle\rho k\rangle \right]_{t=t_0}}_{T_T(t_0)}, \quad (5.8)$$

where τ_0 and δ'_0 are expressed in terms of h_m and δ_I using (2.50) and (2.51). The two terms on the right-hand side of (5.8) represent length and velocity scaling contributions, respectively.

The terms of (5.8) are computed from T0 data, normalized by $\rho_0 (Ag)^{3/2} h_p^{1/2}$, and shown in figure 4(b). Both T_S and T_T contribute substantially to the estimate of the time derivative, with T_S being important near the edges of the mixing layer and T_T dominating near the core. The sum of both terms underestimates the time derivative, with a maximum difference of 17 % at $x_2 \approx \delta_I$. Since the SRT equations are derived on the assumption of

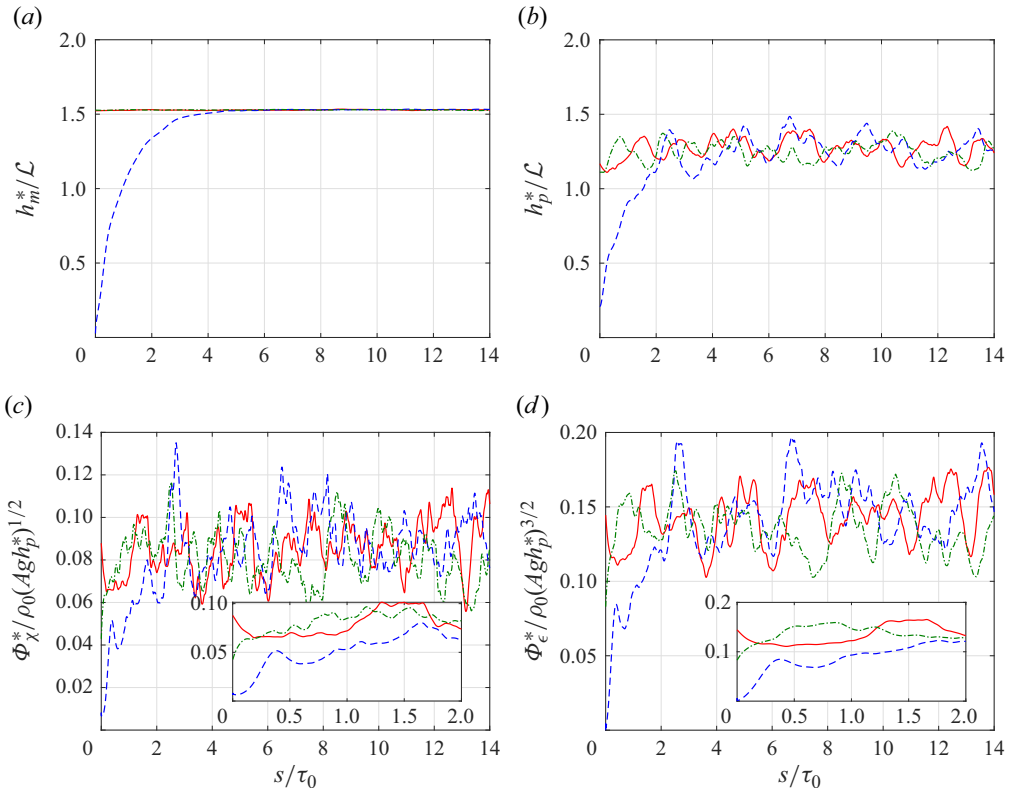


Figure 5. Evolution of normalized (a) mixing height, (b) product height, (c) scalar dissipation integral and (d) viscous dissipation integral for different initial conditions. Insets are zoomed in on early times to highlight differences in the initial transient. The initial conditions used in the SRT cases (I1–I3) correspond respectively to: TRT (red solid); perturbed flat interface (blue dashed); and lower Gr SRT (green dash-dotted).

self-similarity in velocity, it is not surprising that the SRT terms underestimate the time derivative of T_0 , a flow that is experiencing faster-than-self-similar velocity growth (see figure 3).

5.2. Stationarity in the SRT configuration

The time evolution of SRT flow is studied using cases I1–I3. These cases have the same $\lambda = 1.5$ and $Gr = 7.4 \times 10^6$, but start from different initial conditions, as detailed in § 4.2.

Figure 5(a,b) shows different height definitions that represent the large-scale growth of the mixing layer, while figure 5(c,d) shows the integrated scalar and viscous dissipation, respectively, as representations of the small-scale evolution. In these figures, ensemble averages are estimated with planar averages. After an initial transient, all cases exhibit statistical stationarity in all quantities. Case I1 is initialized with a TRT flow whose mixing height is approximately the input height, hence there are no noticeable changes in any of the quantities computed from I1. Case I2 is initialized as a perturbed flat interface. All quantities in I2 start from small values and grow to their statistically stationary values. Because h_m^* is actively controlled via the update of τ_0 according to closure equation (3.1), it approaches an approximately constant value in a manner consistent with (3.2).

Case	IC description	h_m^*/\mathcal{L}	h_p^*/\mathcal{L}	$\frac{\Phi_\chi^*}{\rho_0(Agh_p^*)^{1/2}}$	$\frac{\Phi_\epsilon^*}{\rho_0(Agh_p^*)^{3/2}}$
I1	TRT	1.5289 ± 0.0004	1.251 ± 0.005	0.0813 ± 0.0009	0.138 ± 0.001
I2	Flat interface	1.5296 ± 0.0007	1.248 ± 0.019	0.0827 ± 0.0019	0.139 ± 0.004
I3	Low Gr SRT	1.5291 ± 0.0005	1.254 ± 0.011	0.0827 ± 0.0013	0.139 ± 0.002

Table 4. Effect of initial conditions on SRT for $Gr = 7.4 \times 10^6$, $\lambda = 1.5$.

In contrast, h_p^* responds via the flow dynamics of the SRT equations and oscillates to a greater extent. Case I3 is initialized with an SRT flow of the same height but a smaller Gr . The dissipation integrals start from smaller values, but take less than one τ_0 to grow to their stationary values. Beyond $5\tau_0$, all three signals are indistinguishable. The time-averaged results for $s > 5\tau_0$ are summarized in table 4, with uncertainties computed using the method presented in Rah & Blanquart (2019). It is clear that the stationary solution does not depend on the initial conditions.

These results have two practical implications. First, because the initial conditions of an SRT flow do not affect its stationary solution, initializations may be chosen to maximize efficiency without regard for their effect on the final results. Second, leveraging flow stationarity, all ensemble quantities that are extracted from SRT simulations are averaged in both homogeneous directions and time. Each SRT simulation is performed for at least $50\tau_0$ and statistics are collected after $5\tau_0$. Mathematically, $\langle \cdot \rangle_{SRT} = \langle \cdot \rangle_{1,3,s>5\tau_0}$.

5.3. Validity of the SRT equations

Three key assumptions are used in the derivation of the SRT equations. Assumption (III) was verified in § 5.1 through stationarity in $\alpha(t)$; assumption (II) was verified in § 5.2 through stationarity of all flow quantities in the SRT configuration. In this section, the validity of assumption (I) is assessed. To justify assumption (I), we first propose a candidate for how large this ‘small window of time’ needs to be, then quantify the errors incurred by the SRT simplifications over this time window.

5.3.1. Integral time scale

In § 5.2, it is shown that the flow loses memory of its initial conditions. Stated differently, the flow field loses its time correlation. To quantify how quickly this occurs, temporal autocorrelation functions and integral time scales of several global quantities are computed from I1. These are computed from SRT simulations, as the flow must be statistically stationary and sampled over long times. The temporal autocorrelation function for a general time-varying quantity $F^*(s)$ is

$$R(\tau) = \frac{\langle F^*(s + \tau)F^*(s) \rangle_s}{\langle F^{*2} \rangle_s}. \quad (5.9)$$

Autocorrelation functions are computed and shown in figure 6(a) for $F^* = h_p^*$, K^* , Φ_ϵ^* and Φ_χ^* . All quantities become significantly uncorrelated by $\tau \approx \tau_0$. To quantify this more specifically, integral time scales are computed for each of these functions.

The integral time scale is defined as $\tau_{int} = \int_0^\infty R(\tau) d\tau$. Since these time signals (and their autocorrelation functions) have finite lengths, τ_{int} is estimated with an integral up to

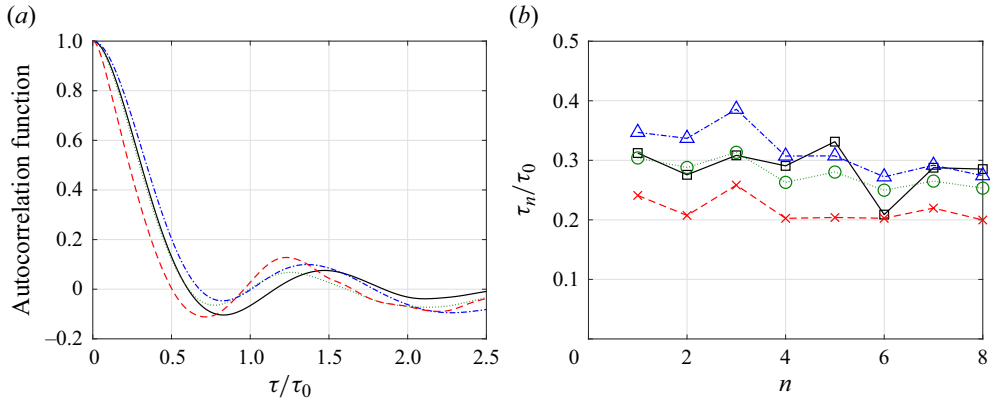


Figure 6. (a) Autocorrelation functions from simulation I1 and (b) corresponding integral time scales computed as the integral of $R(\tau)$ up to the n th zero crossing. Legend: h_p^* (black solid line, squares); K^* (blue dash-dotted, triangles); Φ_ϵ^* (green dotted, circles); and Φ_χ^* (red dashed, crosses).

the n th zero crossing of the autocorrelation function, $\tau_{int} \approx \tau_n$. The integral time scale of each quantity is estimated for varying n and shown in figure 6(b). In general, τ_n varies with the choice of quantity and decreases slowly with n . A conservative upper bound is taken as $\tau_{int} \approx 0.4\tau_0$. After τ_{int} , flow states become uncorrelated, and a subsequent, independent realization of the flow begins. Hence, the SRT approximations need to be valid for a time window bounded by $t_0 \pm \tau_{int}/2$.

5.3.2. Error in mixed mass transport and kinetic energy

Recall that the SRT equations are derived from the NSE in § 2.2 through two main steps. The original NSE, (2.1)–(2.3), are first transformed to the rescaled NSE, (2.23)–(2.25), then simplified to the final SRT equations, (2.33)–(2.35), by evaluating them at $q(t) = q_0$ based on assumption (I). Assessing the validity of assumption (I) is equivalent to quantifying the magnitude of the terms that are neglected even though $q \neq q_0$. The SRT errors in mixed mass and kinetic energy transport are estimated by comparing the budget terms evaluated at $q(t_0 \pm \tau_{int}/2)$ (rescaled TRT) with those at $q(t_0)$ (SRT).

First, assumption (III) is used to relate $q(t_0 \pm \tau_{int}/2)/q_0$ to τ_{int}/τ_0 . Differentiating (2.32) in time yields $q'' = 2\alpha_q A g$, and $q^{(n)} = 0$ for $n > 2$. The function $q(t)$ can be written as an exact Taylor series, which leads to

$$\frac{q(t_0 \pm \tau_{int}/2)}{q_0} = \frac{1}{q_0} \left(q_0 \pm q'_0 \frac{\tau_{int}}{2} + q''_0 \frac{\tau_{int}^2}{8} \right) = 1 \pm \frac{1}{2} \frac{\tau_{int}}{\tau_0} + \frac{1}{16} \left(\frac{\tau_{int}}{\tau_0} \right)^2. \quad (5.10)$$

Substituting $\tau_{int}/\tau_0 = 0.4$, we obtain $0.81 \leq q/q_0 \leq 1.21$.

The SRT errors in mixed mass and kinetic energy budgets are estimated by comparing budgets for the RNSE ($0.81 \leq q(t)/q_0 \leq 1.21$) and the SRT equations ($q = q_0$). The full RNSE budgets and their derivations are found in Appendix E. They are concisely stated as

$$\frac{\partial \langle \rho^* m^* \rangle}{\partial s} = -\frac{\partial \langle \rho^* m^* u_2^* \rangle}{\partial \xi_2} + \frac{\partial}{\partial \xi_2} \left\langle \rho^* D \frac{\partial m^*}{\partial \xi_2} \right\rangle + \langle \rho^* \chi^* \rangle + \left(\frac{\xi_2}{\tau_0} + \delta'_0 \right) \frac{\partial \langle \rho^* m^* \rangle}{\partial \xi_2} + H_m(t), \quad (5.11)$$

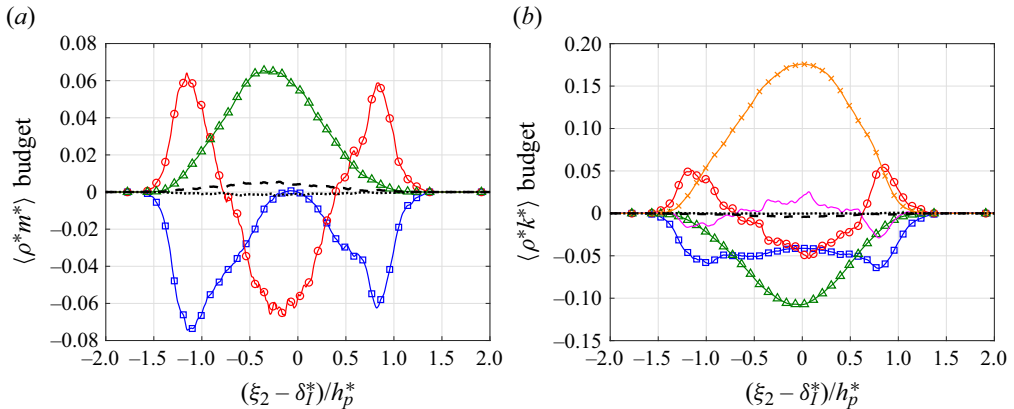


Figure 7. Comparison of SRT budgets with their $q(t)$ -dependent errors: (a) mixed mass, normalized by $\rho_0(Ag/h_p^*)^{1/2}$: convection (red circles); scalar dissipation (green triangles); SRT source term (blue squares); mixed mass diffusion is negligible (not shown). (b) Kinetic energy, normalized by $\rho_0(Ag)^{3/2}h_p^{*1/2}$: convection (red circles); viscous dissipation (green triangles); SRT source terms (blue squares); production (orange crosses); pressure transport (magenta solid line, no symbols); viscous transport is negligible (not shown). In both panels, dashed and dotted black lines represent the total error for $q/q_0 = 0.81$ and 1.21 , respectively.

$$\begin{aligned} \frac{\partial \langle \rho^* k^* \rangle}{\partial s} = & -\frac{\partial \langle \rho^* k^* u_2^* \rangle}{\partial \xi_2} - \left\langle u_i^* \frac{\partial p^*}{\partial \xi_i} \right\rangle + \frac{\partial \langle u_i^* \tau_{i2}^* \rangle}{\partial \xi_2} - \langle \rho^* \epsilon^* \rangle - \langle (\rho^* - \langle \rho^* \rangle) u_2^* \rangle g \\ & + \left(\frac{\xi_2}{\tau_0} + \delta_0' \right) \frac{\partial \langle \rho^* k^* \rangle}{\partial \xi_2} - \frac{\langle \rho^* k^* \rangle}{\tau_0} + H_k(t). \end{aligned} \quad (5.12)$$

The first four terms on the right-hand side of (5.11) constitute the full SRT ($q = q_0$) mixed mass budget. They represent convective transport, diffusive transport, scalar dissipation and the SRT source terms contribution, respectively. The first seven terms on the right-hand side of (5.12) constitute the full SRT kinetic energy budget. They represent convective transport, pressure transport, viscous transport, viscous dissipation, production by buoyancy, and source term contributions from length and velocity scaling, respectively. The final term of each budget equation, H_m and H_k , is the only term that depends on $q(t)$, and represents the error of the SRT equations. In figure 7(a,b), these error terms are compared with their corresponding SRT budget terms and shown to be much smaller for both budgets considered. Therefore, they can be neglected without significant impact on the overall flow dynamics.

6. Results: flow physics

Finally, the SRT flow configuration is leveraged to study the effect of various physical inputs. In § 3, four non-dimensional physical inputs were identified. In this section, the Atwood and Schmidt numbers are held constant to facilitate comparisons with Cabot & Cook (2006), while the effects of the mixing layer aspect ratio and the Grashof number are presented.

6.1. Effect of mixing layer aspect ratio

The effect of mixing layer aspect ratio, $\lambda = \bar{h}_m/\mathcal{L}$, on SRT is shown qualitatively in figure 8. At all λ considered, the two reservoirs of pure heavy and light fluid are separated

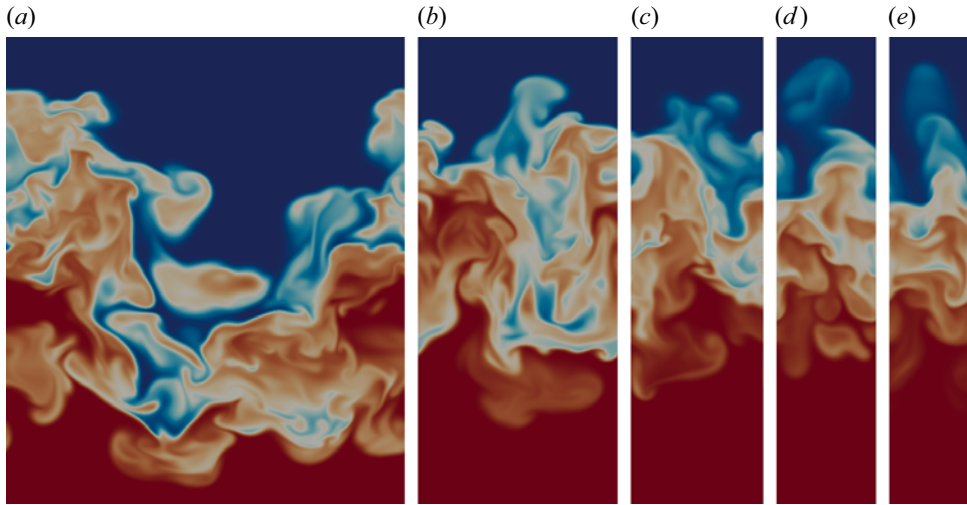


Figure 8. Density fields for SRT cases L1–L5 at $Gr = 7.4 \times 10^6$, with increasing mixing layer aspect ratios from left to right: $\lambda = 0.5, 1.0, 1.5, 2.0, 2.5$. Images are rescaled to have the same h_m^* , and non-mixed regions of the flow in the vertical direction are intentionally removed. Blue and red regions correspond to ρ_H and ρ_L , respectively.

by a highly mixed region that exhibits three-dimensional, random and multiscale features commonly observed in turbulent flows. Consistently, the largest flow structures appear to occupy the entire lateral domain width. For wider (small λ) configurations, sharp interfaces between pockets of heavy and light fluid are evident in many areas, a feature that disappears with enhanced mixing observed in the narrower (large λ) configurations.

The role of the lateral domain size \mathcal{L} is different in TRT and SRT flows. In self-similar TRT flow, Zhou & Cabot (2019) showed that both vertical and horizontal length scales of the flow grow at approximately fixed ratios to the mixing layer height. The TRT flow configuration is solved over a finite time, and domains can be chosen to be sufficiently large (relative to the finite time window) so that they do not affect the flow. Unlike TRT, SRT flow is designed to be simulated over infinitely long times. Vertical growth is restricted by \bar{h}_m but lateral growth is not; horizontal length scales can grow continuously until they are constrained by the lateral domain width if there are no other fluid dynamical constraining mechanisms. As lateral length scales approach the size of the domain, the flow physics is affected by the periodic lateral boundaries. In other stationary configurations of both isotropic (Rosales & Meneveau 2005; Dhandapani & Blanquart 2020) and buoyant (Chung & Pullin 2010; Carroll & Blanquart 2015) turbulent flows, integral turbulence length scales have similarly been shown to depend on the domain dimensions.

To quantify this behaviour, additional flow length scales, similar to Zhou & Cabot (2019), are computed. The correlation length Λ_i^* is defined as the integral of the longitudinal autocorrelation function, i.e.

$$\Lambda_i^* = \int_0^\infty C_i(r) \, dr, \quad C_i(r) = \frac{\langle u_i^{*'}(s, \xi + \mathbf{e}_i r) u_i^{*'}(s, \xi) \rangle}{\langle u_i^{*'} \rangle^2}, \quad (6.1a,b)$$

with no sum over index i (where $i = 1, 2$ or 3), and $u_i^{*'} = u_i^* - \langle u_i^* \rangle$. Since the flow is periodic in ξ_1 and ξ_3 , the horizontal correlation lengths can be defined in terms of their

energy spectra as

$$L_i^* = \int_0^\infty \kappa^{-1} E_i^*(\kappa) d\kappa \Big/ \int_0^\infty E_i^*(\kappa) d\kappa, \quad (6.2)$$

where $E_i^*(\kappa)$ is the two-dimensional spectral energy density of u_i^* , and κ is the two-dimensional wavenumber in the horizontal plane. To characterize the layer core, L_1^* and L_3^* are computed on the ξ_2 -plane closest to δ_1^* . Zhou & Cabot (2019) verified that definitions (6.1) and (6.2) are approximately equivalent, hence, Λ_i^* and L_i^* can be treated interchangeably in the horizontal directions.

The correlation lengths are shown in figure 9(a,b) as a function of λ . The normalized correlation lengths in both the vertical and horizontal directions decrease as the mixing layer aspect ratio is increased. Consistent with visual observations in figure 8, the lateral domain size physically restricts the growth of horizontal length scales in the SRT configuration. A less obvious consequence is that the vertical correlation length also decreases in a similar fashion, despite being normalized by the mixing layer height. Unlike TRT, SRT flow is affected independently by a second large length scale, \mathcal{L} . Hence, a mapping of SRT domain length scales to observed flow length scales is necessary for comparison with TRT.

Time-averaged TRT values (corresponding to $Re > 3000$) for Λ_2 and $L_{1,3}$ are extracted from figure 13 of Zhou & Cabot (2019) and T0. Due to significant statistical variation, these are shown as maximum and minimum values in figure 9. Figure 9(a) shows that Λ_2/h_p from both TRT sources are well matched by SRT at $\lambda = 1.5$. Figure 9(b) shows a much larger spread of $L_{1,3}/h_p$ values from the TRT data. Arguably, all $L_{1,3}^*/h_p^*$ values from the SRT simulations of $0.5 \leq \lambda \leq 2.0$ are within the statistical variation of the two TRT simulations. There are two reasons for this larger statistical variation. First, $L_{1,3}$ is computed from spectra on a single plane, it is expected to be less converged than Λ_2 , which is computed from an integral over the full domain. Second, in both Zhou & Cabot (2019) and T0, it is observed that $L_{1,3}/h_p$ continues to decrease slowly with time. Because the matching of $L_{1,3}/h_p$ values is inconclusive, the excellent agreement in Λ_2/h_p is the main criterion for selecting $\lambda = 1.5$ as the SRT configuration that corresponds best with TRT growth.

Additionally, supporting evidence of the $\lambda = 1.5$ SRT configuration being an equivalent flow unit to self-similar TRT can be found in the spectra of Cabot & Cook (2006). A wavenumber corresponding to the peaks of the vertical velocity and density spectra, k_{peak} , is extracted from figure 2 of Cabot & Cook (2006) and used to estimate an aspect ratio, $h_p k_{peak} / 2\pi \approx 1.2$. This compares well with the value of $h_p^*/\mathcal{L} \approx 1.25$ for SRT at $\lambda = 1.5$. Hence, it appears that the lateral domain width of the SRT configuration may be dynamically equivalent to the most energetic lateral wavelength in TRT flow.

Finally, the effect of the mixing layer aspect ratio is examined in terms of the growth parameter α_p^* and mixedness Ξ^* . Although SRT is statistically stationary, a growth parameter, $\alpha_m^* = \alpha_m(t_0)$, corresponding to a TRT mixing layer at $h_m(t_0)$ can be computed using the SRT parameter τ_0 . Evaluating the definition of α_m at $t = t_0$, and using (2.50), we can relate the TRT growth parameter to SRT flow quantities with

$$\alpha_m^* = \alpha_m(t_0) = \frac{1}{4Ag} \frac{\dot{h}_m^2}{h_m} \Big|_{t=t_0} = \frac{h_m^*}{4Ag} \left(\frac{1}{\tau_0} \right)^2. \quad (6.3)$$

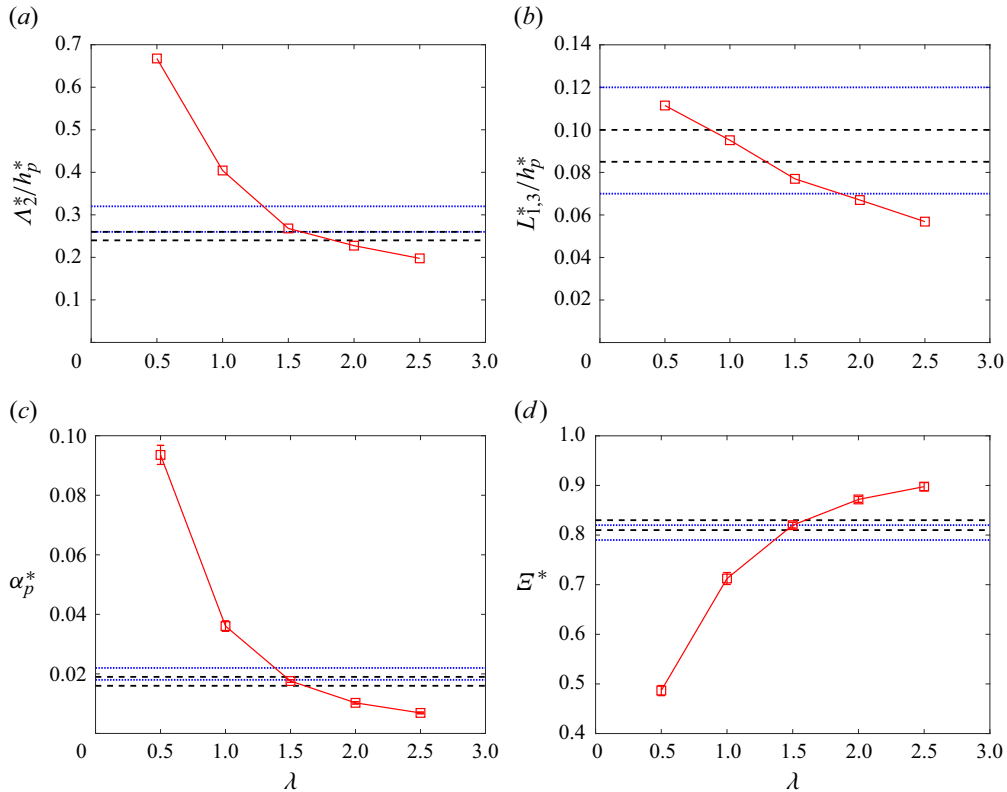


Figure 9. Effect of mixing layer aspect ratio on normalized (a) vertical and (b) horizontal correlation lengths, (c) growth and (d) mixedness parameters. Red markers represent SRT values at $Gr = 7.4 \times 10^6$; the maximum and minimum values from TRT simulations ($Re > 3000$) are shown as: T0 (black dashed); reference dataset (Cabot & Cook 2006; Zhou & Cabot 2019) (blue dotted).

It is then corrected for different height definitions using

$$\alpha_i^* = \alpha_m^* \frac{h_i^*}{h_m^*} = \frac{h_i^*}{4Ag} \left(\frac{1}{\tau_0} \right)^2. \quad (6.4)$$

The mixedness parameter for TRT is defined in (5.2) and Ξ^* has an identical definition, differing only in the coordinate system used. Figure 9(c,d) shows that the SRT values at $\lambda = 1.5$ match self-similar TRT values from Cabot & Cook (2006) and T0 well, verifying that SRT can reproduce TRT flow statistics as long as the correlation lengths are matched.

By matching the statistical flow length scales between SRT and TRT, we identify the SRT configuration with $\lambda = 1.5$ as being representative of self-similar TRT flow (for $A = 0.5$ and $Sc = 1$). This is verified by good agreement in α_p and Ξ^* values. This configuration will be referred to as SRT-1.5 in the subsequent sections.

6.2. Effect of Grashof/Reynolds number

The effect of Grashof number on SRT-1.5 is studied. As discussed in § 3.2, $Gr \propto Re^2$ for a self-similar flow, and either quantity can be used to characterize turbulence intensity. Since Re is more commonly used in TRT studies, all results are presented in terms of Re (defined in (1.4) and (3.7)) for ease of comparison. The $*$ superscript may be omitted

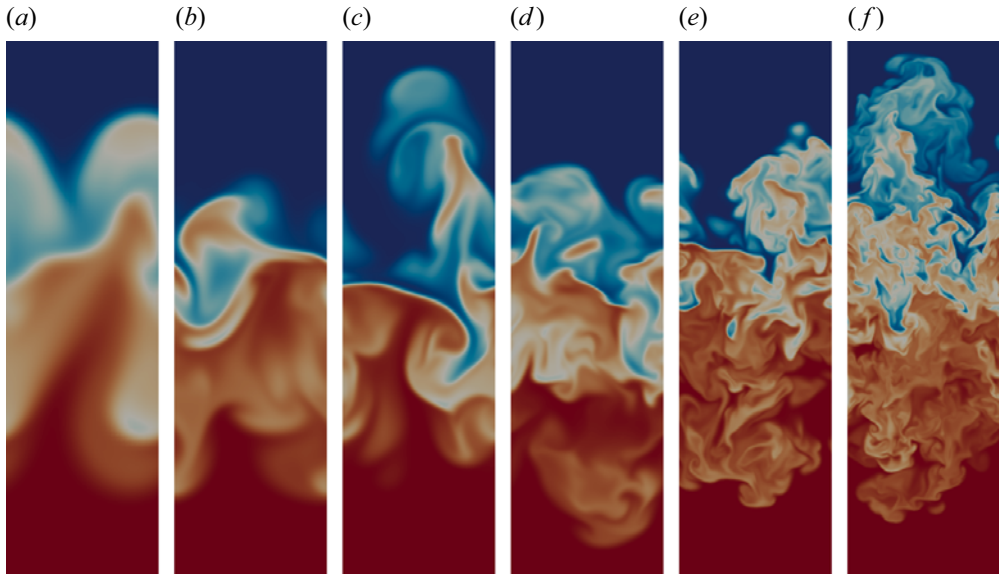


Figure 10. Density fields for SRT cases G1–G6 at $\lambda = 1.5$ and increasing Reynolds (or Grashof) number from left to right: $Re \approx 500, 1200, 1800, 2700, 6400$ and 10800 . Non-mixed regions of the flow in the vertical direction are intentionally removed. Blue and red regions correspond to ρ_H and ρ_L , respectively.

when comparing SRT and TRT quantities, as the specific definition should be clear from the context.

The effect of Re (or Gr) on SRT flow is shown qualitatively in figure 10. All cases have the same \bar{h}_m and \mathcal{L} . Visually, the largest length scales observed are similar across all Reynolds numbers. Expectedly, the largest vertical scale is constrained by \bar{h}_m and the largest horizontal scale is constrained by \mathcal{L} . In contrast, the smallest length scales in the flow decrease noticeably with Reynolds number. Additionally, three-dimensional mixing is observed across all Re . For small Re , this mixing primarily manifests through a smearing of the large-scale interfaces via laminar diffusion. For large Re , this mixing process is driven by the generation of small-scale turbulent structures.

Figure 11 shows the variation of several key parameters with Re for both SRT and TRT flow. Besides α_p and \mathcal{E} , we examine two other parameters, $K/\delta P$ and η . The ratio of kinetic-to-potential energy is defined using the vertically integrated kinetic energy $K(t)$ and the loss of potential energy relative to the initial state:

$$\delta P(t) = \int_{-\infty}^{\infty} \langle \rho(x, t=0) - \rho(x, t) \rangle g x_2 \, dx_2 \quad (6.5)$$

$$\approx g \left[\int_0^{\infty} \langle \rho_H - \rho \rangle x_2 \, dx_2 + \int_{-\infty}^0 \langle \rho_L - \rho \rangle x_2 \, dx_2 - \frac{\rho_H - \rho_L}{2} \delta_I^2 \right]. \quad (6.6)$$

We compute δP using (6.6), which is exactly equal to (6.5) if the initial interface is assumed to be infinitely thin. The corresponding definitions of K^* and δP^* for SRT are similar, with the appropriate variable substitution. The Kolmogorov length scale η presented in figure 11(d) is the minimum value of η found in the mixing layer. It is normalized by the mixing layer height and compared against the expected Kolmogorov scaling.

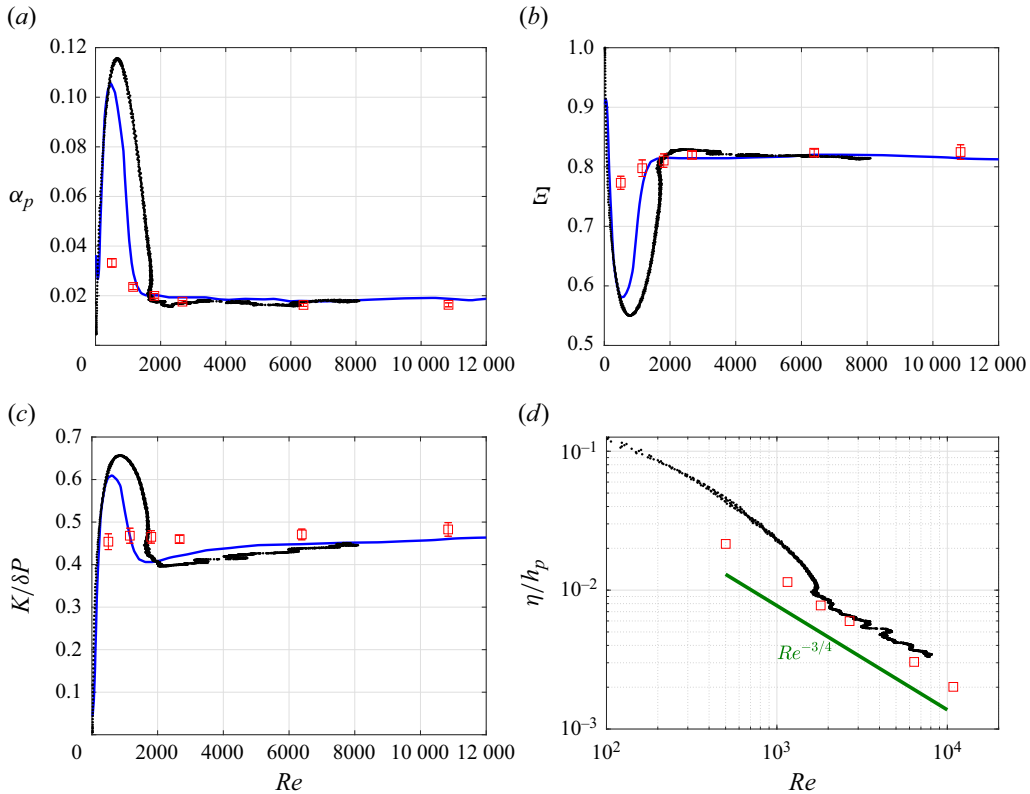


Figure 11. Comparison of SRT-1.5 with two different sources of TRT as a function of Reynolds number: SRT-1.5 (red squares); TRT-T0 (black points); data extracted from Cabot & Cook (2006) (blue solid line). (a) Growth parameter; (b) mixedness; (c) ratio of kinetic to potential energy; (d) normalized Kolmogorov length scale ($Re^{-3/4}$ line represents Kolmogorov scaling).

Both SRT and TRT approach similar behaviour at high Reynolds numbers. The parameters α_p and \mathcal{E} approach statistically stationary values, $K/\delta P$ exhibits a slow growth and η scales in accordance with Kolmogorov scaling. We note that both sets of TRT data predict a lower $K/\delta P$ than SRT-1.5 and exhibit slightly faster growth than SRT-1.5 for $Re > 2000$; it is likely that both TRT simulations have not achieved self-similarity in velocity. This will be addressed in greater detail in § 6.3. While the general high Re behaviour between SRT and TRT flow is similar, the manner in which this self-similar state is approached is drastically different. A distinct change in flow regime is observed at $Re \approx 2000$ for TRT, corresponding to the onset of self-similar growth discussed in § 5.1.1. In contrast, the values in SRT approach high Re behaviour smoothly. Because SRT is independent of initial conditions and enforces self-similar behaviour through timewise recycling, SRT flow decouples memory effects from Re effects, leading to the possibility of low Reynolds number self-similar RT mixing.

6.3. Detailed comparisons between SRT and TRT turbulence

In this section, a more detailed comparison of SRT-1.5 and TRT is performed. We first present planar-averaged statistics for G1–G6 to examine Re effects, then proceed to

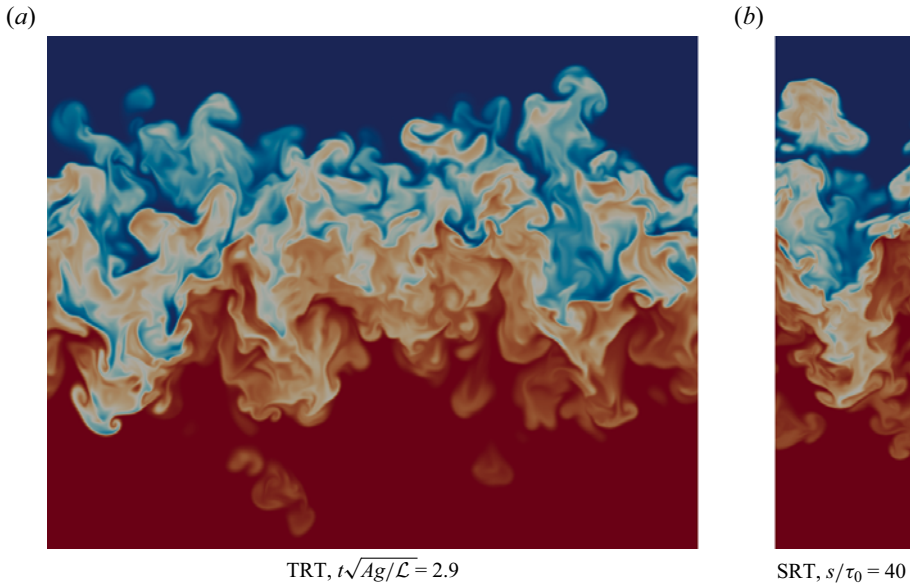


Figure 12. Comparison of TRT-T0 and SRT-1.5 (G5) density fields for $Re \approx 6400$. Images are rescaled to have the same h_m , and non-mixed regions of the flow in the vertical direction are intentionally removed.

compare self-similar results from G5, T0 and the Cabot & Cook (2006) dataset where available.

It was shown in § 6.2 that the global quantities of both TRT and SRT-1.5 show minimal Reynolds number sensitivity for $Re \gtrsim 3000$. We compare G5 ($Re^* \approx 6400$) and the self-similar region of T0 ($3000 \lesssim Re \lesssim 8000$). Statistics from T0 are first normalized, then averaged over this time window. Although the reference dataset has a much larger Re range that reaches up to 32 000, we expect the results between all three simulations to compare relatively well after quantities are suitably normalized. One-dimensional profiles are extracted from Livescu *et al.* (2009) when available. Due to the limited number of snapshots presented, an approximate spread corresponding to all data in the range $Re > 3000$ is shown. This spread represents the maximum and minimum values of the normalized profiles observed at each x_2 location.

A qualitative comparison of SRT-1.5 and TRT-T0 density fields at $Re \approx 6400$ is shown in figure 12. Both flow fields look similar, revealing a similar range of length scales and flow features. Movie 1 shows the time evolution for case G5. After the flow evolves from its lower Gr initial state to higher Gr behaviour by $s \approx \tau_0$, the flow appears stationary, ergodic and similar to TRT flow. Additionally, we note that the mixing layer aspect ratio for SRT-1.5 is approximately 4 times that of the TRT configuration. For the same Re , each in-plane direction for SRT flow is 4 times smaller, resulting in a sixteenfold reduction in the total number of grid points. This has obvious computational benefits that will be further discussed in § 7.2.

The average heavy fluid mole fraction profiles are compared between SRT-1.5 and TRT. Figure 13(a) shows the variation of $\langle X \rangle$ with Reynolds number for SRT-1.5. These profiles show almost no sensitivity to Re , even at very low Reynolds numbers. Case G5 is compared with TRT results in figure 13(b). There are minor differences in the shape of these profiles, with both sources of TRT data having slightly extended tails towards the outer edges of the mixing layer. Next, the average local mixed mass is considered. The variation of

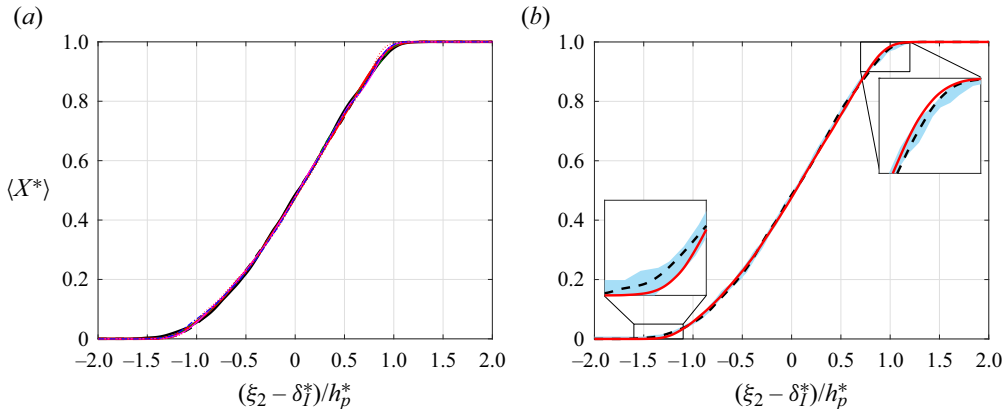


Figure 13. Heavy fluid mole fraction. (a) Reynolds number effects on SRT-1.5 at $Re^* \approx 500$ (red dotted), 1200 (blue dash-dotted), 1800 (magenta solid), 2700 (green dashed), 6400 (thick red solid) and 10800 (thick black dashed). (b) Comparison of SRT-G5 (red), TRT-T0 (black dashed) and approximate spread from Livescu *et al.* (2009) (blue shaded).

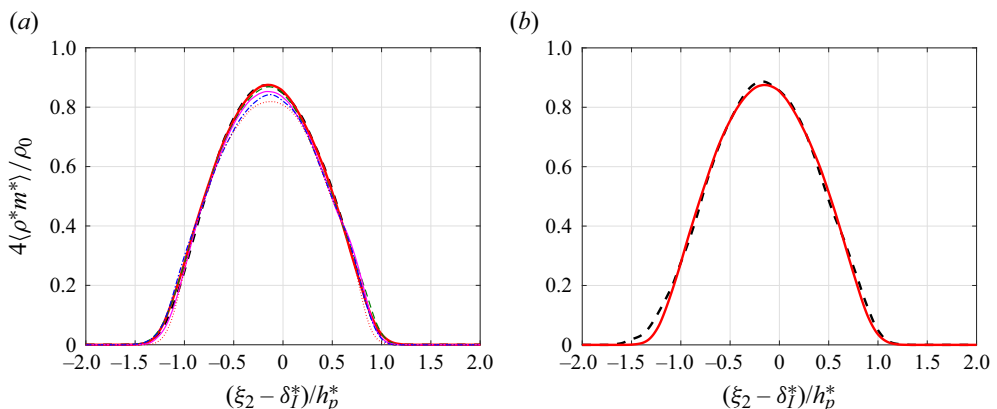


Figure 14. Normalized mixed mass. (a) Reynolds number effects on SRT-1.5 at $Re^* \approx 500$ (red dotted), 1200 (blue dash-dotted), 1800 (magenta solid), 2700 (green dashed), 6400 (thick red solid) and 10800 (thick black dashed). (b) Comparison of SRT-1.5 G5 (red) and TRT-T0 (black dashed).

mixed mass with Reynolds number for SRT-1.5 is shown in figure 14(a). Profile shapes are similar across different Re . Magnitudes are within 5 % across the entire range and converge smoothly towards high Re . Figure 14(b) shows that the average local mixed mass of TRT-T0 compares well with SRT-1.5, but with minor deviations at the tails similar to figure 13(b).

The differences at the outer edges of the mixing layer may be attributed to a deviation from self-similarity in TRT flow. In TRT flow, the outer edges of the mixing layer are characterized by a small number of isolated mushroom-shaped structures with laminar fronts that extend primarily in a single direction (bubbles move up; spikes move down). Examples of these isolated structures are noticeable in the TRT snapshot towards the bottom of figure 12. These structures are most likely to retain some properties of the initial conditions. In contrast, SRT flow retains no memory of the initial perturbations and self-similar mixing is experienced throughout the entire domain.

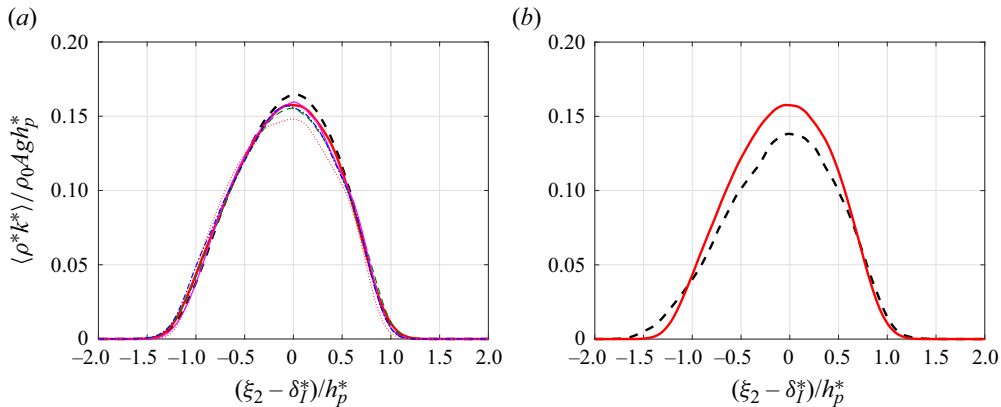


Figure 15. Normalized kinetic energy. (a) Reynolds number effects on SRT-1.5 at $Re^* \approx 500$ (red dotted), 1200 (blue dash-dotted), 1800 (magenta solid), 2700 (green dashed), 6400 (thick red solid) and 10 800 (thick black dashed). (b) Comparison of SRT-G5 (red) and TRT-T0 (black dashed).

Next, the normalized planar-averaged kinetic energy is considered. Figure 15(a,b) shows the Re dependence of SRT-1.5 and a comparison with TRT, respectively. Shapes of kinetic energy profiles are largely similar across Re but there appears to be a weak Re dependence in the peak magnitudes. In figure 15(b), SRT-1.5 is compared with T0 at a similar Reynolds number. Similar to trends observed in the scalar statistics, SRT-1.5 has shorter tails than T0. Additionally, the peak magnitude is 14 % larger than the corresponding value from T0. Although figure 15(b) compares only G5 with T0, it can be easily compared with figure 15(a) to show that T0 has a lower peak than SRT-1.5 for the entire range of Re . This is consistent with the smaller values of $K/\delta P$ for TRT across all $Re > 2000$ in figure 11(c). This discrepancy might be attributed to the fact that the SRT equations are designed to enforce velocity self-similarity, but T0 has not in fact reached a state of velocity self-similarity. It was shown in § 5.1 that normalized velocity statistics continue to grow for T0. It is likely that the SRT-1.5 kinetic energy profiles represent an upper limit for TRT and the profiles for TRT may eventually converge to this limit if T0 is simulated for a longer time window.

Finally, we consider the anisotropy of the velocity field using the anisotropy tensor

$$b_{ij} = \frac{\langle \rho u_i u_j \rangle}{\langle \rho u_k u_k \rangle} - \frac{1}{3} \delta_{ij}, \quad (6.7)$$

of which, the b_{22} component is shown in figure 16(a,b). A value of 0 describes isotropic behaviour and a value of 2/3 represents pure one-dimensional vertical flow. Equation (6.7) involves a ratio of velocities, and these approach zero in the reservoirs. Hence, values of b_{22} near and beyond the edges of the mixing layer should not be overly scrutinized. Figure 16(a) shows that anisotropy increases toward the outer edges of the mixing layer and decreases with Re . In the layer core, b_{22} converges to approximately 0.27 at high Reynolds number. Although magnitudes differ, profile shapes are similar even at low Re and converge smoothly toward high Re . In figure 16(b), the anisotropy of SRT-1.5 is compared with TRT. Both sources of TRT data have slightly larger values of b_{22} compared with SRT-1.5. However, trends are similar and magnitudes are not significantly different. In addition, because the velocity statistics of the TRT simulations may not yet be fully self-similar, it is possible that the anisotropy of the TRT cases could converge to SRT-1.5 values with longer simulation times.

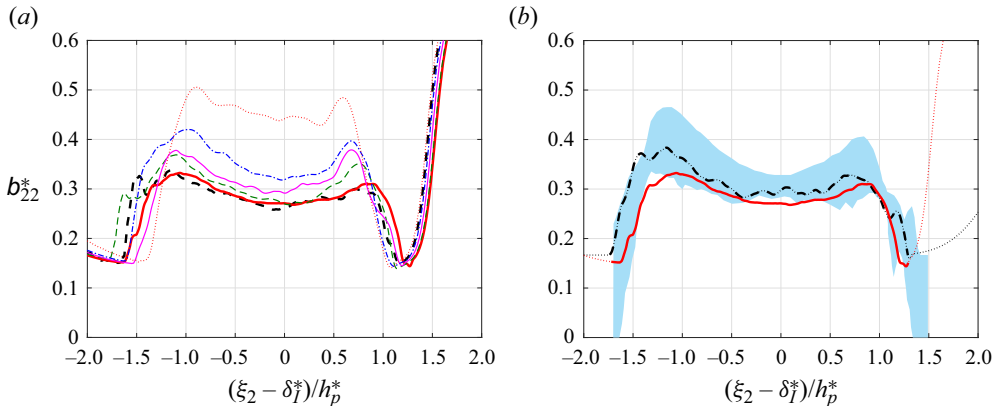


Figure 16. Anisotropy. (a) Reynolds number effects on SRT-1.5 at $Re^* \approx 500$ (red dotted), 1200 (blue dash-dotted), 1800 (magenta solid), 2700 (green dashed), 6400 (thick red solid) and 10 800 (thick black dashed). (b) Comparison of SRT-G5 (red), TRT-T0 (black dashed) and approximate spread from Livescu *et al.* (2009) (blue shaded).

6.4. Higher-order statistics

To verify that the SRT framework preserves the spatial structure of RT turbulence, two-point statistics are considered. Two-dimensional spectra $E_i(\kappa)$ are computed using SRT-G5 data at $x_2 = \delta_I$ (or $\xi_2 = \delta_I^*$), where $E_i(\kappa)$ is the two-dimensional spectral energy density of u_i , and κ is the two-dimensional wavenumber in the horizontal plane. The spectrum for vertical velocity is E_2 , and the spectrum for horizontal velocity is computed as $(E_1 + E_3)/2$. Equivalent spectra are computed from TRT-T0 for a similar $Re \approx 6400$ and both sets of data are compared in figure 17(a). The SRT and TRT spectra show good agreement throughout the entire range of scales. Consistent with Cabot & Cook (2006), an inertial range resembling Kolmogorov $\kappa^{-5/3}$ scaling is observed in the E_2 spectrum, but not in the horizontal directions. The smallest wavenumber in the SRT spectra is approximately four times as large as that of TRT, due to the difference in domain sizes. The smallest wavenumber in SRT flow corresponds exactly to the most energetic wavenumber of TRT flow. This observation is not a coincidence; the SRT configuration acts as a minimum flow unit for RT turbulence, and this will be discussed in § 7.1.

The structure of the small scales is further examined using the anisotropy spectrum

$$B_i(\kappa) = \frac{E_i}{E_1 + E_2 + E_3} - \frac{1}{3}, \quad (6.8)$$

and computed from SRT-G5 and TRT-T0 data. The two spectra are shown in figure 17(b), alongside an approximate spread of the equivalent spectrum for the Cabot & Cook (2006) dataset that is found in figure 13 of Chung & Pullin (2010). All three sets of data seem to suggest an increase in anisotropy in the dissipation range towards the smaller scales, albeit with some differences in magnitudes. The values from SRT-G5 are bounded by those of TRT-T0 and the reference data, verifying that SRT flow reproduces similar spectra to TRT flow. Differences in the two sets of TRT results may be related to initial conditions and/or Reynolds number, but it is difficult to conclude without further study.

Finally, we verify that SRT flow can also capture localized, irregular behaviour by comparing its intermittency characteristics with TRT flow. A procedure similar to Boffetta *et al.* (2009) is used. In one dimension, the p th-order longitudinal velocity structure function is

$$S_p(r) = \langle (u_i(x_i + r) - u_i(x_i))^p \rangle. \quad (6.9)$$

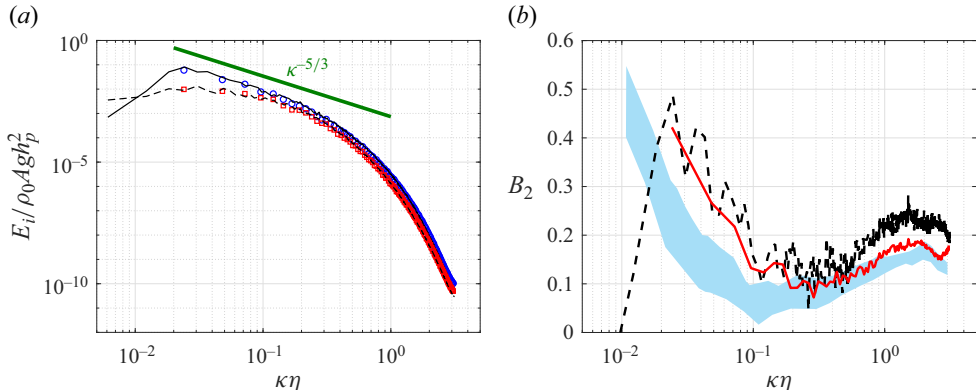


Figure 17. Spectra comparison between TRT-T0 and SRT-G5 at $Re \approx 6400$ on horizontal plane $x_2 \approx \delta_I$. (a) Two-dimensional spectra for vertical and horizontal velocities: TRT E_2 (black solid); TRT $(E_1 + E_3)/2$ (black dashed); SRT E_2^* (blue circles); SRT $(E_1^* + E_3^*)/2$ (red squares). (b) Anisotropy spectra: TRT (black dashed); SRT (red solid); and approximate spread from Chung & Pullin (2010) at $Re \approx 32000$ (blue shaded).

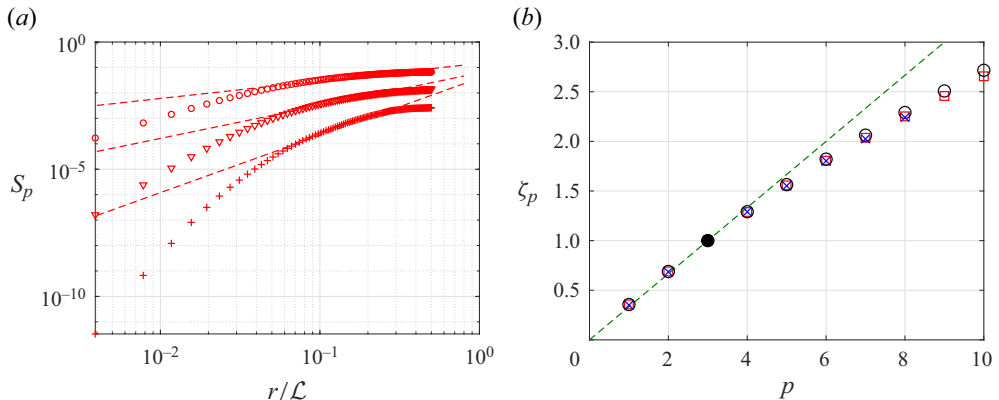


Figure 18. (a) Longitudinal velocity structure functions for $p = 2$ (circles), 4 (triangles) and 8 (plus signs) for SRT-G5 at $\xi_2 = \delta_I^*$. Symbols represent SRT data and dashed lines correspond to the scaling exponents $3\zeta_p/p = 1.0, 0.97$ and 0.84 , respectively. (b) Relative scaling exponents computed using the ESS method based on their deviation from $S_3(r)$: SRT-G5 (red squares); TRT-T0 (black circles); data from Boffetta *et al.* (2009) (blue crosses); Kolmogorov's four-fifth law (dashed green line); assumed $\zeta_3 = 1$ (filled symbol).

These are computed at $x_2 \approx \delta_I$ using $u_1(x_1)$ and $u_3(x_3)$, and averaged over the plane in both horizontal directions. The structure functions for $p = 2, 4$ and 8 are shown in figure 18(a).

Turbulence intermittency can be quantified by computing the scaling exponents, $S_p(r) \propto r^{\zeta_p}$, from the data. A deviation of ζ_p from $p/3$ is commonly considered evidence of turbulence intermittency (Anselmet *et al.* 1984; Meneveau & Sreenivasan 1987). However, obtaining these scaling exponents requires power-law fitting over the limited inertial ranges that are found in the current simulations. The extended self-similarity (ESS) procedure from Benzi *et al.* (1993) is used to overcome this issue. The premise of this procedure is that the dissipation range can also be used in the power-law fitting after it is normalized by the third-order structure function. In doing so, $\zeta_3 = 1$ is assumed.

The computed relative scaling exponents are shown in figure 18(b) for both SRT-G5 and TRT-T0, and the respective fits are reflected in figure 18(a) for comparison with the original SRT structure functions. The scaling exponents from SRT-G5 and TRT-T0

show good agreement, suggesting that SRT flow is able to capture a similar level of intermittency that is present in TRT flow. Although Boffetta *et al.* (2009) studied the RT configuration at a much lower Atwood number (in the Boussinesq approximation), the scaling exponents are extracted from figure 4 of their study and shown in figure 18(b) for comparison purposes. There is little difference between all the results compared, suggesting that Atwood number may not affect the scaling exponents of the structure functions significantly.

7. Discussion

In § 7, a comparison of the TRT and SRT frameworks is considered from two broad perspectives. First, the physical relationship between SRT and TRT flows is explored in § 7.1. Then, the computational benefits of the SRT configuration are discussed in § 7.2.

7.1. Minimal flow unit for self-similar RT turbulence

The results reviewed in § 6 suggest that the SRT configuration with $\lambda = 1.5$ represents a minimal flow unit for self-similar TRT turbulence in the mode-coupling limit. The idea of a ‘minimal flow unit’ has mostly been used in the context of wall-bounded turbulence (Jiménez & Moin 1991; Hamilton, Kim & Waleffe 1995; Hsieh & Biringen 2016), and is extended analogously to the RT configuration here. This flow unit is considered ‘minimal’ because the $\lambda = 1.5$ domain isolates a single unit of the largest energetic structures present in self-similar RT turbulence, as illustrated by the spectra in figure 17(a).

The relatively high aspect ratio SRT minimal flow unit proposed here is not a contradiction to existing findings regarding the effect of lateral confinement on TRT flow (Dalziel *et al.* 2008; Boffetta *et al.* 2012a). In TRT flow, \mathcal{L}_{TRT} is a fixed physical domain. In contrast, \mathcal{L}_{SRT} is a simulation domain that is always scaled by the height of the mixing layer, and unrelated to any physical domain in the TRT sense. As $s \rightarrow \infty$, flow structures in the SRT configuration have a tendency to fill out the lateral domain while maintaining a statistically stationary height. Flow stationarity is expected only after the onset of lateral confinement effects. The SRT minimal flow unit leverages the expected lateral confinement effects to select the aspect ratios of RT flow structures and ‘recycles’ them at a constant aspect ratio. In the context of a self-similar TRT flow, many statistically equivalent realizations of $\lambda = 1.5$ units are tiled horizontally (figure 19). Each of them can be imagined to be expanding at constant aspect ratio, interacting and merging with other neighbouring units to form larger $\lambda = 1.5$ units. In a finite-domain TRT set-up, these units grow in size and eventually experience confinement effects as $h_m(t) \sim \mathcal{L}_{TRT}$. Because \mathcal{L}_{SRT} scales with h_m , the SRT configuration preserves the aspect ratio of these flow units and shields them from any such physical confinement effects, effectively simulating RT turbulence in an infinitely large physical domain.

The SRT-1.5 flow unit represents a theoretical limit at which all memory of initial conditions has been lost, and the physical domain is infinite. Any TRT simulation has to be done on a finite domain over finite time, and it remains questionable if any existing TRT simulation in the literature (as large as they already are) has achieved ‘true’ mode-coupling self-similarity, particularly in velocity statistics. The SRT-1.5 configuration is not a substitute for TRT simulations in all scenarios, especially when the initial conditions or finite-domain effects are of specific interest. It is a configuration for studying late-time self-similar TRT behaviour, and does so using the smallest possible domain.

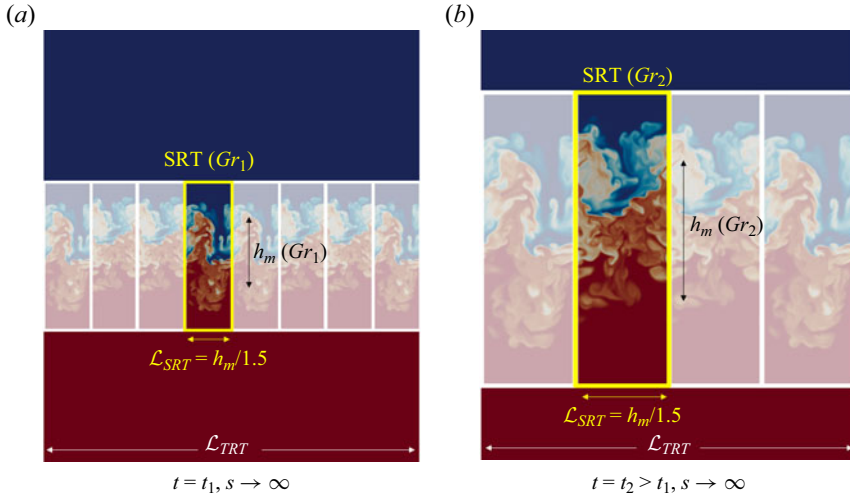


Figure 19. Illustration of the relationship between SRT-1.5 and a finite-domain TRT flow: at an earlier time, t_1 , TRT can be represented as a large number of small SRT units of $\lambda = 1.5$, $Gr = Gr_1$. There is sufficient scale separation ($\mathcal{L}_{TRT} \gg \mathcal{L}_{SRT}$) to allow for constant aspect ratio growth; at late times, fewer and larger SRT units of $Gr_2 > Gr_1$ fit within the finite TRT domain. As \mathcal{L}_{SRT} approaches \mathcal{L}_{TRT} , lateral confinement effects begin to modify the nature of RT turbulence.

7.2. Computational benefits

Lastly, we address the computational benefits that are associated with the SRT configuration.

At a given Reynolds number, the computational cost for one timestep at one grid point is marginally higher in the SRT flow configuration. The evaluation of $\tau_0(s)$, $\delta'_0(s)$ and the associated source terms increases the computational time by $<1\%$. The temporal resolution requirements for both the TRT and SRT configurations are similar. By computing S_ϕ using (4.1), all additional terms are either evaluated semi-implicitly or are stabilizing at large time scales. Time resolution is determined by the convective CFL condition, which is comparable between SRT and TRT, given the similarity in velocity statistics. The small penalty associated with the computation of the additional SRT terms is far outweighed by the benefits listed below:

- (i) Reduced domain size: for the same layer height, the SRT minimal flow unit identified in § 6.1 requires a lateral domain width that is approximately one-fourth that of the TRT simulation reported in Cabot & Cook (2006), which translates to a sixteenfold reduction in the total number of grid points for an equivalent flow condition. Granted, due to the smaller number of grid points in each snapshot, multiple snapshots will be required to reach a similar level of statistical convergence. However, memory requirements are significantly reduced and there is greater flexibility in storage and analysis of the data.
- (ii) Independence of initial conditions: each TRT simulation has to be initialized from a perturbed flat interface and evolved over its full time history. Unlike TRT flow, SRT flow has been shown in § 5.2 to be insensitive to initial conditions. Hence, thoughtful flow initialization strategies, such as using an existing turbulent simulation of a different Re as an initial condition, can speed up convergence to the target flow state.
- (iii) Convergence of ensemble statistics: when simulating TRT flow on a finite domain, self-similarity only develops after an initial transient, and the flow eventually

experiences lateral confinement effects. There is a limited time window (if any) for the collection of self-similar TRT statistics. The number of statistical samples can only be increased by using a larger domain or by performing multiple realizations of the same simulation. In contrast, SRT flow is stationary and ergodic. A single flow configuration can theoretically be simulated over infinite time on the same grid to generate an infinite number of realizations, guaranteeing converged estimates of ensemble statistics.

- (iv) Reduced Re requirements for self-similar RT turbulence: finally, self-similar turbulence can be observed robustly at a much lower Reynolds number in SRT flows than in TRT flows. The effects of initial conditions and Reynolds number are intrinsically linked in TRT flow. In contrast, the SRT configuration encourages self-similar behaviour and decouples the two effects, yielding unique statistically stationary solutions defined entirely by A , Sc , Gr and λ . This is true even at low Re (or Gr). Additionally, the results in § 6 show that low Re SRT turbulence is qualitatively similar to high Re cases and approaches the high Re limit in a smooth, monotonic fashion. This property makes the SRT configuration a highly scalable test bed for the development of turbulence models for buoyancy-driven flows.

8. Conclusion

Inspired by the observed self-similar behaviour of RT mixing layers, a coordinate transformation was applied to the low-Mach-number NSE to obtain a new set of equations in the rescaled coordinate system. The rescaled governing equations, referred to as the SRT equations, are valid in the vicinity of a fixed time. These equations resemble the original NSE but contain two sets of additional terms; one arises from rescaling of the vertical coordinate and takes a similar form in the continuity, momentum and scalar equations; the second arises from rescaling of velocities and only appears in the momentum equation.

Using the SRT equations, we demonstrated that self-similar TRT turbulence in the mode-coupling limit can be simulated in a statistically stationary manner, circumventing many of the computational challenges typically associated with temporally growing simulations. A minimum flow unit for self-similar RT turbulence (SRT-1.5) was identified, which reveals the underlying structure of such flows. The results from SRT-1.5 match well with TRT simulations, and differences can likely be attributed to the non-self-similar nature of the TRT simulations considered. We propose that SRT-1.5 generates RT turbulence at a theoretical limit corresponding to complete flow self-similarity. This may otherwise only be achieved through TRT simulations with longer times and larger grids than any existing simulation.

Supplementary movie. Supplementary movie is available at <https://doi.org/10.1017/jfm.2024.1104>.

Acknowledgements. The authors acknowledge the Texas Advanced Computing Center (TACC) at The University of Texas at Austin for providing computational resources that have contributed to the research results reported within this paper. URL: <http://www.tacc.utexas.edu>.

Funding. This material is based upon work supported by the National Science Foundation under Grant No. 2422513.

Declaration of interests. The authors report no conflict of interest.

Author ORCIDs.

- ② Chian Yeh Goh <https://orcid.org/0009-0007-1426-7581>;
- ② Guillaume Blanquart <https://orcid.org/0000-0002-5074-9728>.

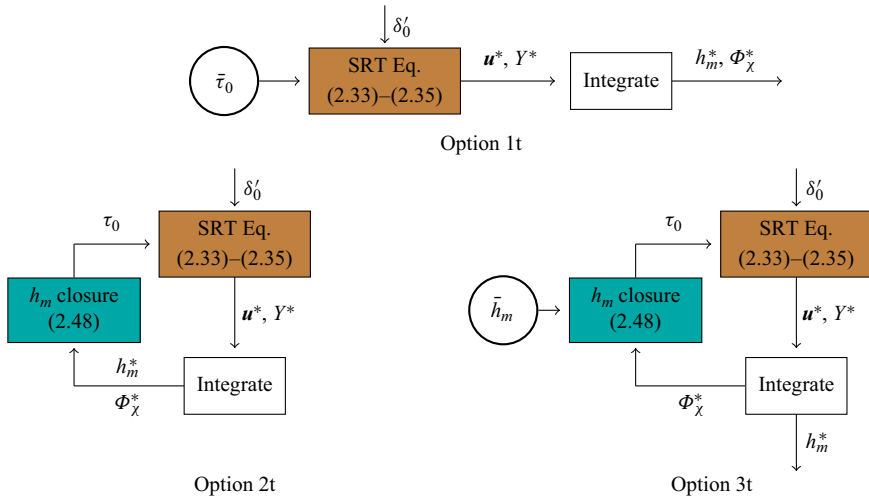


Figure 20. Options for implementing τ_0 . Quantities with an overbar (circled) are prescribed constant inputs.

Appendix A. Implementation of SRT inputs

The complete SRT equations are defined by (2.33)–(2.35) and require the specification of two parameters τ_0 and δ'_0 . After a statistically stationary state is reached, we expect (2.44) and (2.48) to be satisfied. In this section, we outline several options for how this stationary state can be reached through different ways of implementing τ_0 and δ'_0 .

A.1. Choice of τ_0 : stability of h_m^*

The options for implementing τ_0 are summarized in figure 20. Option 1t uses a prescribed constant $\bar{\tau}_0$ as input to the SRT equations. Both options 2t and 3t use (2.48), with option 2t enforcing instantaneous stationarity, and option 3t driving the flow toward a stationary state at a particular mixing height. We examine the stability of the stationary solution using the h_m^* time-evolution equation.

- (i) Constant τ_0 as direct input (option 1t): when a constant value, $\bar{\tau}_0 > 0$, is used directly as an input to (2.33)–(2.35), the time evolution of h_m^* can be derived by substituting $\tau_0 = \bar{\tau}_0$ into (2.47) to yield

$$\frac{dh_m^*}{ds} = \frac{4}{\rho_0} \Phi_\chi^* - \frac{1}{\bar{\tau}_0} h_m^*. \quad (\text{A1})$$

Because $\bar{\tau}_0$ and h_m^* are both positive by definition, the last term on the right-hand side of (A1) is a relaxation term that stabilizes h_m^* . Φ_χ^* is positive by definition, hence the first term is destabilizing. The overall stability of h_m^* depends on the relative scaling of both terms on the right-hand side. In general, this is dependent on the flow physics.

- (ii) Enforcing instantaneous stationarity (option 2t): the second option uses the stationarity relation derived in § 2.3 to enforce $dh_m^*/ds = 0$ at all times. This is achieved by updating $\tau_0(s)$ continuously based on (2.48) as

$$\frac{1}{\tau_0(s)} = \frac{4\Phi_\chi^*(s)}{\rho_0 h_m^*(s)}. \quad (\text{A2})$$

Because stationarity is satisfied at all times, h_m^* is completely determined, at least analytically, by its initial state and can only be changed by re-initializing the flow. Moreover, while stationarity is satisfied analytically, it may not be satisfied numerically. Errors may accumulate and h_m^* may drift from its initial value.

(iii) Constant mixing height as input (option 3t): finally, option 3t uses a constant mixing width, $\bar{h}_m > 0$, as input to the stationarity relation such that $\tau_0(s)$ is continuously updated as

$$\frac{1}{\tau_0(s)} = \frac{4\Phi_\chi^*(s)}{\rho_0 \bar{h}_m}. \quad (\text{A3})$$

Substituting (A3) into (2.47) gives

$$\frac{dh_m^*}{ds} = \frac{4\Phi_\chi^*}{\rho_0} \left(1 - \frac{h_m^*}{\bar{h}_m} \right). \quad (\text{A4})$$

Both Φ_χ^* and h_m^* are positive by definition. This guarantees the relaxation of the instantaneous layer width to the prescribed target value, $h_m^*(s) \rightarrow \bar{h}_m$, regardless of its initial state.

Option 3t is chosen as the input method because it guarantees stability and affords the user flexibility to prescribe a target mixing height that is independent of initial conditions. Practically, an input length scale \bar{h}_m is also preferred to an input time scale $\bar{\tau}_0$ because \bar{h}_m can be easily compared with computational (e.g. grid, domain size) and physical length scales (e.g. Kolmogorov scale, other height definitions) when setting up the simulation.

A.2. Choice of δ'_0 : stability of δ_I^*

The options for implementing δ'_0 , illustrated in figure 21, are analogous to the ones for τ_0 . We examine the stability of the stationary solution using the δ_I^* time evolution equation.

(i) Constant δ'_0 as direct input (option 1d): one way to implement δ'_0 is to use a constant input $\bar{\delta}'_0$ directly with the SRT equations. Equation (2.43) becomes

$$\frac{d\delta_I^*}{ds} = -\frac{1}{\tau_0} \delta_I^* - \bar{\delta}'_0. \quad (\text{A5})$$

Because $1/\tau_0 > 0$, this is a stable equation and

$$\delta_I^*(s) \rightarrow -\bar{\delta}'_0 \tau_0(s). \quad (\text{A6})$$

The parameter $\tau_0(s)$ is, in general, a time-varying quantity. Hence, $\delta_I^*(s)$ converges to a time-varying quantity in the statistically stationary state.

(ii) Enforcing instantaneous stationarity (option 2d): a second option is to enforce stationarity in δ_I^* instantaneously using (2.44) such that $d\delta_I^*/ds = 0$ for all time, i.e.

$$\delta'_0(s) = -\frac{1}{\tau_0} \delta_I^*(s). \quad (\text{A7})$$

The considerations against option 2d are the same as those for option 2t.

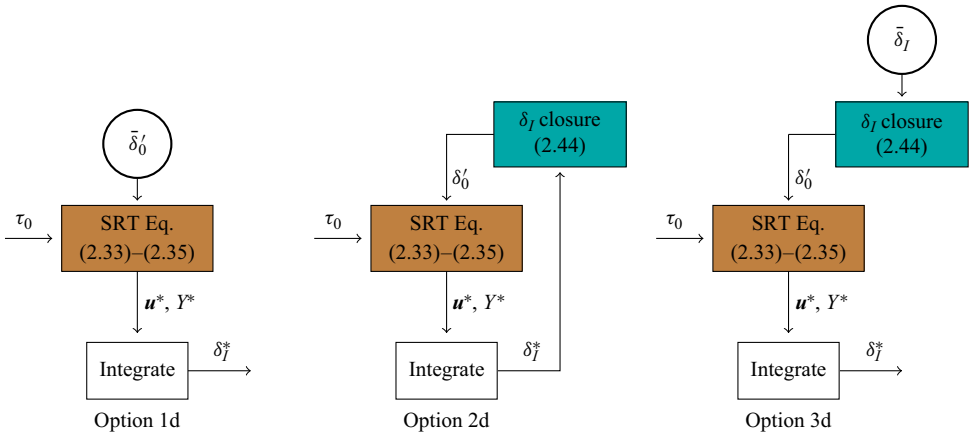


Figure 21. Options for implementing δ'_0 . Quantities with an overbar (circled) are prescribed constant inputs.

(iii) Constant displacement length as input (option 3d): as a third option, we use a constant value for the displacement length, $\bar{\delta}_I$, as input to (2.44), i.e.

$$\delta'_0 = -\frac{1}{\tau_0} \bar{\delta}_I. \quad (\text{A8})$$

Equation (2.43) becomes

$$\frac{d\delta_I^*}{ds} = \frac{1}{\tau_0} (\bar{\delta}_I - \delta_I^*), \quad (\text{A9})$$

which is a stable equation that guarantees $\delta_I^*(s) \rightarrow \bar{\delta}_I$.

Both options 1d and 3d are analytically stable, and enable the mixing layer to be shifted without re-initialization. With option 1d, $\delta_I^*(s)$ (and hence the total mass) fluctuates in the stationary state. Hence, option 3d is preferred because $\delta_I^*(s)$ relaxes to a constant target value that serves as a known reference location for all times.

A.3. Equivalence of implementation options

The choice of implementation does not affect the final result. To demonstrate this, two simulations are compared. Case I1O3 (also I1/K2/L3/G4) is performed using option 3, and a second simulation I1O1 is performed using option 1. Case I1O3 takes $(h_m, \bar{\delta}_I)$ as inputs and computes $(\tau_0(s), \delta'_0(s))$ as outputs, while case I1O1 takes (τ_0, δ'_0) as inputs, and computes $(h_m^*(s), \delta_I^*(s))$ as outputs. To verify their equivalence, the time-averaged values of $\tau_0(s)$ and $\delta'_0(s)$ from I1O3 are used as inputs to I1O1. The time evolution of each of these four quantities is shown in figure 22. For option 3, $(h_m^*(s), \delta_I^*(s))$ approach near-constant values consistent with (A4) and (A9), while $(\tau_0(s), \delta'_0(s))$ oscillate. For option 1, (τ_0, δ'_0) are constants (as prescribed), and $(h_m^*(s), \delta_I^*(s))$ oscillate. These observations are consistent with the time-evolution equations presented in §§ A.1 and A.2.

Despite differences in the timewise behaviour of these particular quantities, the ensemble-averaged results from options 1 and 3 are identical to each other, within statistical uncertainty. These are summarized in table 5. There is a unique solution for ensemble-averaged SRT flow, that is controlled by two additional parameters. These can be height h_m^* and position δ_I^* , or time scale τ_0 and drift δ'_0 . Prescribing either set of inputs maps the other to this unique state, resulting in equivalent flows that are independent of how the simulation is implemented.

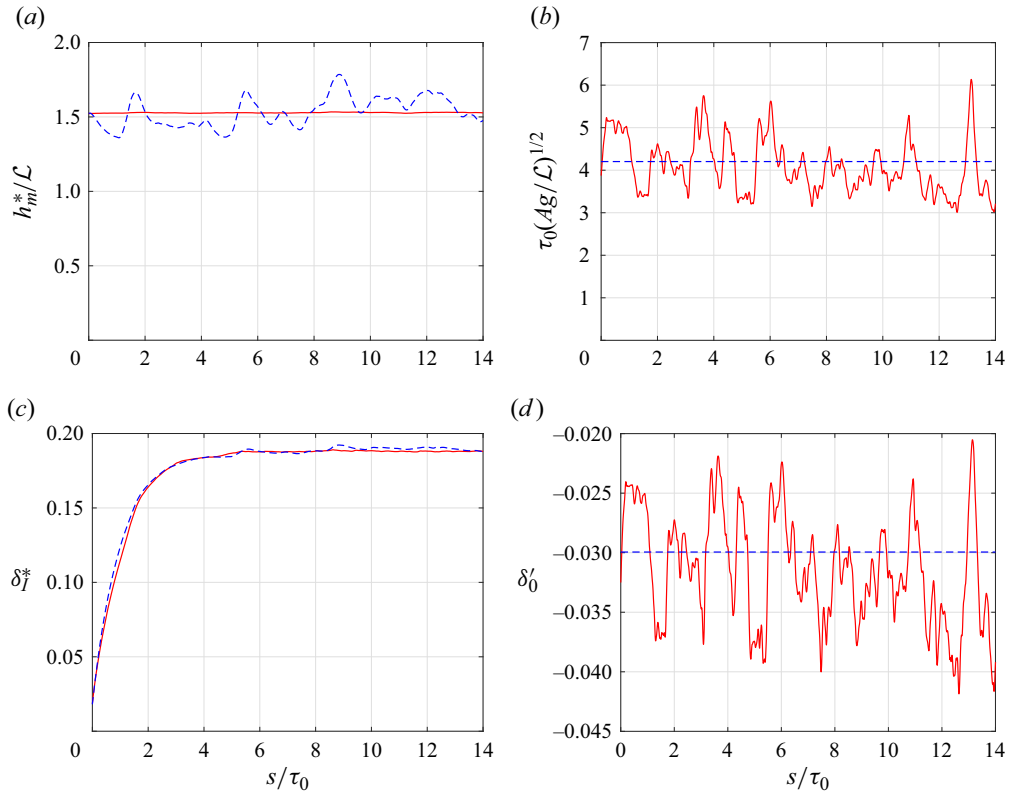


Figure 22. Comparison of option 1 (blue dashed) and option 3 (red solid). (a) Mixing layer height; (b) SRT time scale parameter; (c) displacement length; (d) SRT translation velocity parameter.

Parameter	Option 1	Option 3
$1/\tau_0$	0.168	0.168 ± 0.002
h_m^*	1.54 ± 0.02	1.5289 ± 0.0004
h_p^*	1.26 ± 0.03	1.251 ± 0.005
Φ_χ^*	0.082 ± 0.001	0.0813 ± 0.0009
Φ_ϵ^*	0.139 ± 0.004	0.138 ± 0.001
α_p^*	0.0179 ± 0.0004	0.0177 ± 0.0004
Ξ^*	0.817 ± 0.033	0.819 ± 0.006

Table 5. Comparison of ensemble-averaged results between options 1 and 3.

Appendix B. Detailed simulation parameters

In § 3.2, seven physical inputs (g , ρ_H , ρ_L , v , D , \bar{h}_m , \mathcal{L}) and four independent dimensionless groups (A , Sc , Gr , λ) were identified. Hence, three of the seven input parameters can be arbitrarily chosen. In our simulations, these are $g = \rho_H = \mathcal{L} = 1$. The remaining four inputs are determined from the choice of $A = 0.5$, $Sc = 1$, Gr (varied) and λ (varied). Specific input values and some intermediate outputs are presented in table 6, which serves as an extension to table 3.

Case	Inputs								Outputs				
	\bar{h}_m	δ_I	$v(10^{-5})$	N_1	N_{2c}	N_2	\mathcal{L}_{2c}	\mathcal{L}_2	h_p	h_1	H	Re	$\kappa_{max}\eta^*$
T0	—	—	2.3895	1024	954	1060	0.93	4.27	0.35	0.40	0.70	8000	3.04
I1	1.5	0.178	47.778	128	456	546	3.56	21.1	1.25	1.71	2.75	2669	2.99
I2	1.5	0.178	47.778	128	456	546	3.56	21.1	1.25	1.71	2.73	2666	2.97
I3	1.5	0.178	47.778	128	456	546	3.56	21.1	1.25	1.72	2.75	2713	2.98
K1	1.5	0.178	47.778	64	228	304	3.56	16.1	1.36	1.86	3.06	2669	1.51
K3	1.5	0.178	47.778	256	910	1014	3.55	15.7	1.24	1.69	2.71	2622	5.94
L1	0.5	0.081	9.1949	384	624	720	1.63	7.1	0.68	0.91	1.35	10423	3.06
L2	1.0	0.128	26.007	192	490	582	2.55	11.6	0.95	1.28	1.99	4173	2.95
L4	2.0	0.230	73.559	96	440	530	4.58	21.1	2.14	3.54	3.54	1961	3.10
L5	2.5	0.282	102.85	78	440	530	5.64	25.9	1.89	2.60	4.34	1559	3.25
G1	1.5	0.178	303.37	32	114	176	3.56	16.1	1.32	1.78	2.60	501	2.83
G2	1.5	0.178	120.39	64	228	304	3.56	16.1	1.27	1.73	2.68	1154	2.91
G3	1.5	0.178	70.115	96	342	426	3.56	15.9	1.27	1.73	2.69	1807	2.94
G5	1.5	0.178	18.961	256	910	1014	3.55	15.7	1.25	1.70	2.74	6388	3.04
G6	1.5	0.178	11.042	384	1364	1476	3.55	15.4	1.26	1.72	2.74	10842	3.07

Table 6. Detailed simulation parameters. The T0 outputs are approximate values at the end of the simulation.

Appendix C. Determination of aspect ratio limit for TRT simulation

In TRT simulation T0, the mixing layer aspect ratio (in terms of H/\mathcal{L}) is compared with a threshold value to limit lateral confinement effects. This threshold value is deduced from the final simulation time of Cabot & Cook (2006). However, H/\mathcal{L} was not directly reported and had to be derived from other reported parameters. The ratio H/\mathcal{L} can be expanded as

$$\left(\frac{H}{\mathcal{L}}\right)^3 = \frac{1}{2} \left(\frac{H}{h_p}\right) \left(\frac{H\dot{H}}{v}\right)^2 \left(\frac{\dot{h}_p}{\dot{H}}\right)^2 \left(\frac{4Ag h_p}{\dot{h}_p^2}\right) \left(\frac{v^2}{2Ag \Delta_1^3}\right) \left(\frac{\Delta_1}{\mathcal{L}}\right)^3. \quad (C1)$$

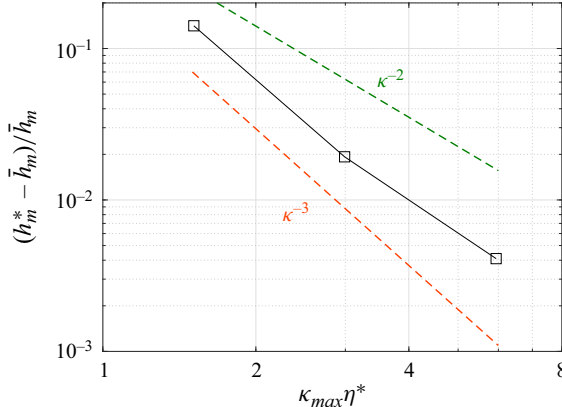
The input computational parameters are quoted explicitly as $Gr_\Delta = (2Ag \Delta_1^3)/v^2 = 1$, and $N = \mathcal{L}/\Delta_1 = 3072$. For a self-similar flow, we assume $\dot{H}/\dot{h}_p \approx H/h_p$. The self-similar parameters are $\alpha_p = \dot{h}_p^2/(4Ag h_p) \approx 0.02$ (extracted from their figure 4) and $H/h_p \approx 2.4$ (reported). At the end of the simulation, $Re = H\dot{H}/v \approx 32000$. Substituting these values into (C1), we find $H/\mathcal{L} \approx 0.72$ at the end of the simulation.

Appendix D. Effect of grid resolution on SRT flow

To assess the effects of grid resolution, a parametric sweep of $\kappa_{max}\eta^* \approx 1.5, 3, 6$ was conducted for constant Gr and λ using K1–K3. Table 7 summarizes the results, and shows that grid resolution has an impact on the output values that exceeds the statistical uncertainty.

Specific attention is placed on h_m^* because it has a known analytical solution. While (3.2) implies that $h_m^* = \bar{h}_m$ in the stationary state, this is not satisfied numerically. The relative deviation of h_m^* from its input value is presented in figure 23. Here, h_m^* is consistently larger than \bar{h}_m and converges towards \bar{h}_m with increased resolution. This error can be attributed

Case	$\kappa_{max}\eta^*$	h_m^*/\mathcal{L}	h_p^*/\mathcal{L}	$\frac{\Phi_\chi^*}{\rho_0(4gh_p^*)^{1/2}}$	$\frac{\Phi_\epsilon^*}{\rho_0(4gh_p^*)^{3/2}}$
K1	1.5	1.7119 ± 0.0022	1.360 ± 0.010	0.0746 ± 0.0014	0.128 ± 0.003
K2	3.0	1.5289 ± 0.0004	1.251 ± 0.005	0.0813 ± 0.0009	0.138 ± 0.001
K3	6.0	1.5061 ± 0.0001	1.235 ± 0.010	0.0815 ± 0.0017	0.138 ± 0.002

 Table 7. Effect of grid resolution on SRT for $Gr = 7.4 \times 10^6$, $\lambda = 1.5$.

 Figure 23. Effect of grid resolution on the deviation of h_m^* from prescribed input, \bar{h}_m . For reference, dashed lines have slopes corresponding to second-order (green) and third-order (orange) accuracy.

to numerical diffusion, which exists in any bounded scalar transport scheme. One may mimic the impact of the numerical diffusion D_{num} by multiplying the molecular diffusion D by a factor $(1 + D_{num}/D)$. Specifically, (2.47) becomes

$$\frac{dh_m^*}{ds} \approx \frac{4}{\rho_0} \left(1 + \frac{D_{num}}{D}\right) \Phi_\chi^* - \frac{1}{\tau_0} h_m^*. \quad (\text{D1})$$

Because $1/\tau_0$ is updated via (3.1), (D1) becomes

$$\frac{dh_m^*}{ds} \approx \frac{4\Phi_\chi^*}{\rho_0} \left(1 + \frac{D_{num}}{D} - \frac{h_m^*}{\bar{h}_m}\right), \quad (\text{D2})$$

and the stationary solution can be written as

$$\frac{D_{num}}{D} \approx \frac{h_m^* - \bar{h}_m}{\bar{h}_m}. \quad (\text{D3})$$

Hence, the relative error in h_m^* can provide an estimate for the numerical scalar diffusion present in the flow. Comparing the errors with the reference slopes in figure 23, the error in h_m^* exhibits second-order convergence. This is consistent with the order of accuracy of the BCH scheme (Verma *et al.* 2014). The BCH scheme was chosen for scalar transport precisely for its reduced numerical diffusion, yet, the numerical diffusivity observed at conventional DNS resolution is significant. Specifically, at $\kappa_{max}\eta^* = 1.5$, numerical diffusion is estimated to be 14 % of physical diffusion. This is expected to be worse with other bounded scalar transport schemes that have larger numerical diffusion. As the grid resolution is increased to $\kappa_{max}\eta^* = 3$, this value is reduced to smaller than 2 %. Taking into

account both results from [table 7](#) and [figure 23](#), $\kappa_{max}\eta^* = 3$ is assessed to be sufficient for this study.

Appendix E. Mixed mass and kinetic energy budgets for rescaled TRT flow

E.1. Mixed mass transport in rescaled TRT flow

The ensemble-averaged mixed mass transport equation for rescaled TRT flow (as opposed to SRT flow) is derived in the same way as [\(2.46\)](#), but starting with the full rescaled scalar equation [\(2.25\)](#), instead of the SRT equation [\(2.35\)](#). All ratios involving q , q' and q'' can be written in terms of q/q_0 using assumption (III), such as

$$\frac{q'}{q'_0} = \left(\frac{q}{q_0}\right)^{1/2}, \quad \frac{q'}{q} = \frac{q'}{q'_0} \frac{q'_0}{q_0} \frac{q_0}{q} = \frac{1}{\tau_0} \left(\frac{q_0}{q}\right)^{1/2}, \quad \frac{q''}{q'} = \frac{1}{2} \frac{q'}{q} = \frac{1}{2\tau_0} \left(\frac{q_0}{q}\right)^{1/2}. \quad (\text{E1a-c})$$

The mixed mass transport equation derived from the RNSE is

$$\begin{aligned} \frac{\partial \langle \rho^* m^* \rangle}{\partial s} = & - \frac{\partial \langle \rho^* m^* u_2^* \rangle}{\partial \xi_2} + \frac{\partial}{\partial \xi_2} \left\langle \rho^* D \frac{\partial m^*}{\partial \xi_2} \right\rangle + \langle \rho^* \chi^* \rangle + \left(\frac{\xi_2}{\tau_0} + \delta'_0 \right) \frac{\partial \langle \rho^* m^* \rangle}{\partial \xi_2} \\ & + H_{c,m} + H_{D,m} + H_\chi + H_{S,m}, \end{aligned} \quad (\text{E2})$$

where the first four terms on the right-hand side represent convective transport, diffusive transport, scalar dissipation and the SRT source terms contribution, respectively. These four terms constitute the full SRT ($q = q_0$) mixed mass budget. The additional $q(t)$ -dependent error terms associated with each of these terms are

$$H_{c,m} = - \left[\left(\frac{q_0}{q} \right)^{1/2} - 1 \right] \frac{\partial \langle \rho^* m^* u_2^* \rangle}{\partial \xi_2}, \quad (\text{E3})$$

$$H_{D,m} = \left[\left(\frac{q_0}{q} \right)^2 - 1 \right] \frac{\partial}{\partial \xi_2} \left\langle \rho^* D \frac{\partial m^*}{\partial \xi_2} \right\rangle, \quad (\text{E4})$$

$$H_\chi = \left[\left(\frac{q_0}{q} \right)^2 - 1 \right] \langle \rho^* \chi^{e*} \rangle, \quad \chi^{e*} = 2D \left(\frac{\partial Y^*}{\partial \xi_2} \right)^2, \quad (\text{E5})$$

$$H_{S,m} = \left[\left(\frac{q_0}{q} \right)^{1/2} - 1 \right] \left(\frac{\xi_2}{\tau_0} + \delta'_0 \right) \frac{\partial \langle \rho^* m^* \rangle}{\partial \xi_2}. \quad (\text{E6})$$

The sum of these error terms is written as H_m in [§ 5.3.2](#). Each term is estimated by assuming that the ensemble averages of the rescaled quantities are constant in time and approximated by SRT flow, i.e. the dominant source of error in time originates from the variation of $q(t)/q_0$.

E.2. Kinetic energy transport in rescaled TRT flow

A similar procedure is used to derive the kinetic energy transport equation for the full RNSE. To isolate dynamical pressure effects from the hydrostatic head, pressure is decomposed into a hydrostatic component and a fluctuating component $p^{* \prime}$ such that

$\partial p^*/\partial \xi_i = \partial p^{*'}/\partial \xi_i - \langle \rho^* \rangle g \delta_{2i}$. The RNSE kinetic energy budget is

$$\begin{aligned} \frac{\partial \langle \rho^* k^* \rangle}{\partial s} = & - \frac{\partial \langle \rho^* k^* u_2^* \rangle}{\partial \xi_2} - \left\langle u_i^* \frac{\partial p^{*'}}{\partial \xi_i} \right\rangle + \frac{\partial \langle u_i^* \tau_{i2}^* \rangle}{\partial \xi_2} - \langle \rho^* \epsilon^* \rangle - \langle (\rho^* - \langle \rho^* \rangle) u_2^* \rangle g \\ & + \left(\frac{\xi_2}{\tau_0} + \delta_0' \right) \frac{\partial \langle \rho^* k^* \rangle}{\partial \xi_2} - \frac{\langle \rho^* k^* \rangle}{\tau_0} \\ & + H_{C,k} + H_{p,k} + H_{v,k} + H_\epsilon + H_{\mathcal{P}} + H_{S,k} + H_{T,k}, \end{aligned} \quad (\text{E7})$$

where the first seven terms on the right-hand side represent convective transport, pressure transport, viscous transport, viscous dissipation, production by buoyancy and source term contributions from length and velocity scaling, respectively. The remaining $q(t)$ -dependent error terms are

$$H_{C,k} = - \left[\left(\frac{q_0}{q} \right)^{1/2} - 1 \right] \frac{\partial \langle \rho^* k^* u_2^* \rangle}{\partial \xi_2}, \quad H_{p,k} = - \left[\left(\frac{q_0}{q} \right)^{1/2} - 1 \right] \left\langle u_i^* \frac{\partial p^*}{\partial \xi_i} \right\rangle, \quad (\text{E8a,b})$$

$$H_{v,k} = \left[\frac{q_0}{q} - 1 \right] \left[\frac{\partial \langle u_i^* (\tau_{i2}^* + \tau_{i2}^{e*}) \rangle}{\partial \xi_2} + \left(\frac{q_0}{q} - 1 \right) \frac{\partial \langle u_i^* \tau_{i2}^{e*} \rangle}{\partial \xi_2} \right], \quad (\text{E9})$$

$$H_\epsilon = - \left[\frac{q_0}{q} - 1 \right] \left[\left\langle \tau_{i2}^* \frac{\partial u_i^*}{\partial \xi_2} + \tau_{ij}^{e*} \frac{\partial u_i^*}{\partial \xi_j} \right\rangle + \left(\frac{q_0}{q} - 1 \right) \left\langle \tau_{i2}^{e*} \frac{\partial u_i^*}{\partial \xi_2} \right\rangle \right], \quad (\text{E10})$$

$$H_{\mathcal{P}} = - \left[\left(\frac{q_0}{q} \right)^{1/2} - 1 \right] \langle (\rho^* - \langle \rho^* \rangle) u_2^* g \rangle, \quad (\text{E11})$$

$$H_{S,k} = \left[\left(\frac{q_0}{q} \right)^{1/2} - 1 \right] \left(\frac{1}{\tau_0} \xi_2 + \delta_0' \right) \frac{\partial \langle \rho^* k^* \rangle}{\partial \xi_2}, \quad H_{T,k} = - \left[\left(\frac{q_0}{q} \right)^{1/2} - 1 \right] \frac{\langle \rho^* k^* \rangle}{\tau_0}. \quad (\text{E12a,b})$$

The sum of these error terms is written as H_k in § 5.3.2. Similar to the mixed mass budget, we approximate that all t -dependent errors are dominated by $q(t)/q_0$.

REFERENCES

ABARZHI, S.I. 2010 Review of theoretical modelling approaches of Rayleigh–Taylor instabilities and turbulent mixing. *Phil. Trans. R. Soc. A* **368** (1916), 1809–1828.

ANDREWS, M.J. & DALZIEL, S.B. 2010 Small Atwood number Rayleigh–Taylor experiments. *Phil. Trans. R. Soc. A* **368** (1916), 1663–1679.

ANSELMET, F., GAGNE, Y., HOPFINGER, E.J. & ANTONIA, R.A. 1984 High-order velocity structure functions in turbulent shear flows. *J. Fluid Mech.* **140**, 63–89.

BANERJEE, A. 2020 Rayleigh–Taylor instability: a status review of experimental designs and measurement diagnostics. *J. Fluids Engng* **142** (12), 120801.

BANERJEE, A. & ANDREWS, M.J. 2006 Statistically steady measurements of Rayleigh–Taylor mixing in a gas channel. *Phys. Fluids* **18** (3), 035107.

BANERJEE, A. & ANDREWS, M.J. 2009 3D simulations to investigate initial condition effects on the growth of Rayleigh–Taylor mixing. *Int. J. Heat Mass Transfer* **52** (17–18), 3906–3917.

BANERJEE, A., GORE, R.A. & ANDREWS, M.J. 2010a Development and validation of a turbulent-mix model for variable-density and compressible flows. *Phys. Rev. E* **82** (4), 046309.

BANERJEE, A., KRAFT, W.N. & ANDREWS, M.J. 2010b Detailed measurements of a statistically steady Rayleigh–Taylor mixing layer from small to high Atwood numbers. *J. Fluid Mech.* **659**, 127–190.

BENZI, R., CILIBERTO, S., TRIPICCIONE, R., BAUDET, C., MASSAIOLI, F. & SUCCI, S. 1993 Extended self-similarity in turbulent flows. *Phys. Rev. E* **48**, R29–R32.

BOFFETTA, G., DE LILLO, F. & MUSACCHIO, S. 2012a Anomalous diffusion in confined turbulent convection. *Phys. Rev. E* **85**, 066322.

BOFFETTA, G., DE LILLO, F., MAZZINO, A. & MUSACCHIO, S. 2012b Bolgiano scale in confined Rayleigh–Taylor turbulence. *J. Fluid Mech.* **690**, 426–440.

BOFFETTA, G. & MAZZINO, A. 2017 Incompressible Rayleigh–Taylor turbulence. *Annu. Rev. Fluid Mech.* **49**, 119–143.

BOFFETTA, G., MAZZINO, A., MUSACCHIO, S. & VOZELLA, L. 2009 Kolmogorov scaling and intermittency in Rayleigh–Taylor turbulence. *Phys. Rev. E* **79** (6), 065301.

BURTON, G.C. 2011 Study of ultrahigh Atwood-number Rayleigh–Taylor mixing dynamics using the nonlinear large-eddy simulation method. *Phys. Fluids* **23** (4), 045106.

CABOT, W.H. & COOK, A.W. 2006 Reynolds number effects on Rayleigh–Taylor instability with possible implications for type-Ia supernovae. *Nat. Phys.* **2**, 562–568.

CABOT, W.H. & ZHOU, Y. 2013 Statistical measurements of scaling and anisotropy of turbulent flows induced by Rayleigh–Taylor instability. *Phys. Fluids* **25** (1), 015107.

CARROLL, P.L. & BLANQUART, G. 2015 A new framework for simulating forced homogeneous buoyant turbulent flows. *Theor. Comput. Fluid Dyn.* **29** (3), 225–244.

CHANDRASEKHAR, S. 1955 The character of the equilibrium of an incompressible heavy viscous fluid of variable density. *Math. Proc. Camb. Phil. Soc.* **51** (1), 162–178.

CHERTKOV, M. 2003 Phenomenology of Rayleigh–Taylor turbulence. *Phys. Rev. Lett.* **91** (11), 115001.

CHUNG, D. & PULLIN, D.I. 2010 Direct numerical simulation and large-eddy simulation of stationary buoyancy-driven turbulence. *J. Fluid Mech.* **643**, 279–308.

COOK, A.W., CABOT, W.H. & MILLER, P.L. 2004 The mixing transition in Rayleigh–Taylor instability. *J. Fluid Mech.* **511**, 333–362.

DALZIEL, S.B., PATTERSON, M.D., CAULFIELD, C.P. & COOMARASWAMY, I.A. 2008 Mixing efficiency in high-aspect-ratio Rayleigh–Taylor experiments. *Phys. Fluids* **20** (6), 065106.

DESIARDINS, O., BLANQUART, G., BALARAC, G. & PITSCHE, H. 2008 High order conservative finite difference scheme for variable density low Mach number turbulent flows. *J. Comput. Phys.* **227** (15), 7125–7159.

DHANDAPANI, C. & BLANQUART, G. 2020 From isotropic turbulence in triply periodic cubic domains to sheared turbulence with inflow/outflow. *Phys. Rev. Fluids* **5** (12), 124605.

DIMONTE, G. & TIPTON, R. 2006 K-L turbulence model for the self-similar growth of the Rayleigh–Taylor and Richtmyer–Meshkov instabilities. *Phys. Fluids* **18** (8), 085101.

DIMONTE, G., *et al.* 2004 A comparative study of the turbulent Rayleigh–Taylor instability using high-resolution three-dimensional numerical simulations: the Alpha-Group collaboration. *Phys. Fluids* **16** (5), 1668–1693.

DUFF, R.E., HARLOW, F.H. & HIRT, C.W. 1962 Effects of diffusion on interface instability between gases. *Phys. Fluids* **5** (4), 417–425.

HAMILTON, J.M., KIM, J. & WALEFFE, F. 1995 Regeneration mechanisms of near-wall turbulence structures. *J. Fluid Mech.* **287**, 317–348.

HSIEH, A. & BIRINGEN, S. 2016 The minimal flow unit in complex turbulent flows. *Phys. Fluids* **28** (12), 125102.

JIMÉNEZ, J. & MOIN, P. 1991 The minimal flow unit in near-wall turbulence. *J. Fluid Mech.* **225**, 213–240.

LIVESCU, D. & RISTORCELLI, J.R. 2007 Buoyancy-driven variable-density turbulence. *J. Fluid Mech.* **591**, 43–71.

LIVESCU, D., RISTORCELLI, J.R., GORE, R.A., DEAN, S.H., CABOT, W.H. & COOK, A.W. 2009 High-Reynolds number Rayleigh–Taylor turbulence. *J. Turbul.* **10**, N13.

LIVESCU, D., WEI, T. & PETERSEN, M.R. 2011 Direct numerical simulations of Rayleigh–Taylor instability. *J. Phys. Conf. Ser.* **318**, 082007.

LUO, T., WANG, Y., YUAN, Z., JIANG, Z., HUANG, W. & WANG, J. 2023 Large-eddy simulations of compressible Rayleigh–Taylor turbulence with miscible fluids using spatial gradient model. *Phys. Fluids* **35** (10), 105131.

MELLADO, J.P., SARKAR, S. & ZHOU, Y. 2005 Large-eddy simulation of Rayleigh–Taylor turbulence with compressible miscible fluids. *Phys. Fluids* **17** (7), 076101.

MENEVEAU, C. & SREENIVASAN, K.R. 1987 The multifractal spectrum of the dissipation field in turbulent flows. *Nucl. Phys. B Proc. Suppl.* **2**, 49–76.

MIKHAEL, M., SUCHANDRA, P., RANJAN, D. & PATHIKONDA, G. 2021 Simultaneous velocity and density measurements of fully developed Rayleigh–Taylor mixing. *Phys. Rev. Fluids* **6** (7), 073902.

MORGAN, B.E., OLSON, B.J., WHITE, J.E. & MCFARLAND, J.A. 2017 Self-similarity of a Rayleigh–Taylor mixing layer at low Atwood number with a multimode initial perturbation. *J. Turbul.* **18** (10), 973–999.

MORGAN, B.E. & WICKETT, M.E. 2015 Three-equation model for the self-similar growth of Rayleigh–Taylor and Richtmyer–Meshkov instabilities. *Phys. Rev. E* **91** (4), 043002.

MUESCHKE, N.J., ANDREWS, M.J. & SCHILLING, O. 2006 Experimental characterization of initial conditions and spatio-temporal evolution of a small-Atwood-number Rayleigh–Taylor mixing layer. *J. Fluid Mech.* **567**, 27–63.

MUESCHKE, N.J. & SCHILLING, O. 2009a Investigation of Rayleigh–Taylor turbulence and mixing using direct numerical simulation with experimentally measured initial conditions. I. Comparison to experimental data. *Phys. Fluids* **21** (1), 014106.

MUESCHKE, N.J. & SCHILLING, O. 2009b Investigation of Rayleigh–Taylor turbulence and mixing using direct numerical simulation with experimentally measured initial conditions. II. Dynamics of transitional flow and mixing statistics. *Phys. Fluids* **21** (1), 014107.

MUESCHKE, N.J., SCHILLING, O., YOUNGS, D.L. & ANDREWS, M.J. 2009 Measurements of molecular mixing in a high-Schmidt-number Rayleigh–Taylor mixing layer. *J. Fluid Mech.* **632**, 17–48.

RAH, K.J. & BLANQUART, G. 2019 Numerical forcing scheme to generate passive scalar mixing on the centerline of turbulent round jets in a triply periodic box. *Phys. Rev. Fluids* **4** (12), 124504.

RAMAPRABHU, P. & ANDREWS, M.J. 2004a Experimental investigation of Rayleigh–Taylor mixing at small Atwood numbers. *J. Fluid Mech.* **502**, 233–271.

RAMAPRABHU, P. & ANDREWS, M.J. 2004b On the initialization of Rayleigh–Taylor simulations. *Phys. Fluids* **16** (8), L59–L62.

RAMAPRABHU, P., DIMONTE, G. & ANDREWS, M.J. 2005 A numerical study of the influence of initial perturbations on the turbulent Rayleigh–Taylor instability. *J. Fluid Mech.* **536**, 285–319.

RAYLEIGH, L. 1882 Investigation of the character of the equilibrium of an incompressible heavy fluid of variable density. *Proc. Lond. Math. Soc.* **s1-14** (1), 170–177.

RISTORCELLI, J.R. & CLARK, T.T. 2004 Rayleigh–Taylor turbulence: self-similar analysis and direct numerical simulations. *J. Fluid Mech.* **507**, 213–253.

ROSALES, C. & MENEVEAU, C. 2005 Linear forcing in numerical simulations of isotropic turbulence: physical space implementations and convergence properties. *Phys. Fluids* **17** (9), 095106.

RUAN, J. & BLANQUART, G. 2021 Direct numerical simulations of a statistically stationary streamwise periodic boundary layer via the homogenized Navier–Stokes equations. *Phys. Rev. Fluids* **6** (2), 024602.

SCHILLING, O. 2020 Progress on understanding Rayleigh–Taylor flow and mixing using synergy between simulation, modeling, and experiment. *J. Fluids Engng* **142** (12), 120802.

SCHILLING, O. 2021 Self-similar Reynolds-averaged mechanical–scalar turbulence models for Rayleigh–Taylor, Richtmyer–Meshkov, and Kelvin–Helmholtz instability-induced mixing in the small Atwood number limit. *Phys. Fluids* **33** (8), 085129.

SCHILLING, O. & MUESCHKE, N.J. 2010 Analysis of turbulent transport and mixing in transitional Rayleigh–Taylor unstable flow using direct numerical simulation data. *Phys. Fluids* **22** (10), 105102.

SCHILLING, O. & MUESCHKE, N.J. 2017 Turbulent transport and mixing in transitional Rayleigh–Taylor unstable flow: A priori assessment of gradient-diffusion and similarity modeling. *Phys. Rev. E* **96** (6), 063111.

TAYLOR, G.I. 1950 The instability of liquid surfaces when accelerated in a direction perpendicular to their planes. I. *Proc. R. Soc. Lond. A* **201** (1065), 192–196.

VERMA, S., XUAN, Y. & BLANQUART, G. 2014 An improved bounded semi-Lagrangian scheme for the turbulent transport of passive scalars. *J. Comput. Phys.* **272**, 1–22.

VLADIMIROVA, N. & CHERTKOV, M. 2009 Self-similarity and universality in Rayleigh–Taylor, Boussinesq turbulence. *Phys. Fluids* **21** (1), 015102.

YILMAZ, I. 2020 Analysis of Rayleigh–Taylor instability at high Atwood numbers using fully implicit, non-dissipative, energy-conserving large eddy simulation algorithm. *Phys. Fluids* **32** (5), 054101.

YOUNGS, D.L. 1984 Numerical simulation of turbulent mixing by Rayleigh–Taylor instability. *Physica D* **12** (1–3), 32–44.

YOUNGS, D.L. 2013 The density ratio dependence of self-similar Rayleigh–Taylor mixing. *Phil. Trans. R. Soc. A* **371** (2003), 20120173.

ZHANG, Y., RUAN, Y., XIE, H. & TIAN, B. 2020 Mixed mass of classical Rayleigh–Taylor mixing at arbitrary density ratios. *Phys. Fluids* **32** (1), 011702.

ZHOU, Y. 2017a Rayleigh–Taylor and Richtmyer–Meshkov instability induced flow, turbulence, and mixing. I. *Phys. Rep.* **720–722**, 1–136.

ZHOU, Y. 2017b Rayleigh–Taylor and Richtmyer–Meshkov instability induced flow, turbulence, and mixing. II. *Phys. Rep.* **723–725**, 1–160.

ZHOU, Y. & CABOT, W.H. 2019 Time-dependent study of anisotropy in Rayleigh–Taylor instability induced turbulent flows with a variety of density ratios. *Phys. Fluids* **31** (8), 084106.

ZHOU, Y., CABOT, W.H. & THORNBER, B. 2016 Asymptotic behavior of the mixed mass in Rayleigh–Taylor and Richtmyer–Meshkov instability induced flows. *Phys. Plasmas* **23** (5), 052712.